Occurrence and development of folding related to normal faulting within a mechanically heterogeneous sedimentary sequence: a case study from Inner Moray Firth, UK

A. Lăpădat[1*], J. Imber[1,2], G. Yielding[2], D. Iacopini[3], K.J.W. McCaffrey[1], J.J. Long[4], R.R. Jones[4]

[1] *Department of Earth Sciences, Durham University, Durham, DH1 3LE, UK*

[2] *Badley Geoscience Ltd., Hundleby, Spilsby, Lincolnshire, PE23 5NB, UK*

[3] *Geology and Petroleum Geology Department, University of Aberdeen, Aberdeen, AB24 3UE, UK*

[4] *Geospatial Research Ltd., Suites 7 & 8, Harrison House, Hawthorne Terrace, Durham, DH1 4EL, UK*

[*] *Corresponding author (e-mail: i.a.lapadat@durham.ac.uk)*

Abbreviated title: Folding related to normal faulting

Abstract

Folds associated with normal faults are potential hydrocarbon traps and may impact the connectivity of faulted reservoirs. Well-calibrated seismic reflection data that image a normal fault system from the Inner Moray Firth basin, offshore Scotland, show that folding was preferentially localized within the mechanically incompetent Lower-Middle Jurassic pre-rift interval, comprising interbedded shales and sandstones, and within Upper Jurassic syn-rift shales. Upward propagation of fault tips was initially inhibited by these weak lithologies, generating fault propagation folds with amplitudes of ~50 m. Folds were also generated, or amplified, by translation of the hangingwall over curved, convex-upward fault planes. These fault bends resulted from vertical fault segmentation and linkage within mechanically incompetent layers. The relative contributions of fault propagation and fault-bend folding to the final fold amplitude may vary significantly along the strike of a single fault array. In areas where opposite-dipping, conjugate normal faults intersect, the displacement maxima are skewed upwards towards the base of the syn-rift sequence (i.e. the free surface at the time of fault initiation) and significant fault propagation folding did not occur. These observations can be explained by high compressive stresses generated in the vicinity of conjugate fault

intersections, which result in asymmetric displacement distributions, skewed toward the upper tip, with high throw gradients enhancing upward fault propagation. Our observations suggest that mechanical interaction between faults, in addition to mechanical stratigraphy, is a key influence on the occurrence of normal fault-related folding, and controls kinematic parameters such as fault propagation/slip ratios and displacement rates.

Introduction

Folding related to normal faulting is mainly the result of fault propagation and linkage at different stages of the growth of normal faults (Withjack et al, 1990; Schlische, 1995; Janecke et al, 1998; Corfield and Sharp, 2000; Sharp et al, 2000; Ferrill et al, 2005; White and Crider, 2006; Jackson et al, 2006; Ferrill et al, 2007; Ferrill et al, 2012; Tvedt et al, 2013; Tavani and Granado, 2015). The main mechanisms generating fault-related folds in extensional domains are: (i) flexural deformation around vertical and lateral tips of propagating blind faults (fault-propagation folding) (Walsh and Watterson, 1987; Ferrill et al, 2005); (ii) folding between overlapping / underlapping, vertically or laterally segmented faults (Rykkelid and Fossen, 2002; Childs et al, this volume; Rotevatn and Jackson, 2014); (iii) translation of the hangingwall over a bend in a fault plane (Groshong, 1989; Xiao and Suppe, 1992; Rotevatn and Jackson, 2014); (iv) distributed shear deformation (Fossen and Hesthammer, 1998; Ferrill et al, 2005); and (v) frictional drag (Davis and Reynolds, 1984). Mechanical properties of the host rocks exert a primary influence on normal fault geometry and development of extensional folds (Ferrill et al, 2007; Ferrill and Morris, 2008; Tvedt et al, 2013). With the help of analogue, numerical and kinematic models (Groshong, 1989; Whitjack et al, 1990; Dula, 1991; Saltzer and Pollard, 1992; Hardy and McClay, 1999; Johnson and Johnson, 2002; Jin and Groshong, 2006), researchers have shown that changes in fault dip, strain rate and thickness of the incompetent layer also control the development of extensional fault-related folds. For example, thick incompetent layers will tend to inhibit fault propagation and promote formation of fault-tip monoclines (Withjack and Callaway, 2000).

Nevertheless, models are constrained by imposed boundary conditions and are usually designed to test a single mechanism. Growth of the faults is a dynamic process in which fault geometry, slip-related stress perturbations and strain rates can vary in both space and time (Cowie, 1998; Gupta and Scholz, 2000) and, as a consequence, different processes might be responsible for the generation of folds during the evolution of a normal fault system. Numerical models, supported by seismological evidence, indicate that faults develop and

interact within heterogeneous stress fields resulting from regional tectonic stress and local stress perturbations (Cowie, 1998; Gupta and Scholz, 2000). This heterogeneity induces local variations in fault slip, fault propagation and strain rates (Willemse et al, 1996; Crider and Pollard, 1998; Gupta et al, 1998; Gupta and Scholz, 2000; Willemse and Pollard, 2000; White and Crider, 2006), key parameters in controlling the development of extensional monoclines (Withjack et al, 2000; Hardy and Allmendinger, 2011). We still know relatively little about the possible influence of heterogeneous stress distributions on the development of fault-related folding (White and Crider, 2006), and have yet to explain the variable occurrence and development of extensional folding along single fault arrays.

In this paper we use 2- and 3D seismic reflection data from the Inner Moray Firth basin, offshore Scotland, to investigate the influence of host-rock lithology, and fault geometry and fault interaction on the development of normal fault-related folds. First, we describe the three-dimensional geometries of the faults and folds using 3D seismic data. We map the fault throw distributions, and describe variations in the thicknesses and geometries of the syn-rift seismic sequences, to interpret the spatial and temporal (i.e. kinematic) evolution of the faults and folds. Next, we augment these observations with interpretations of faults and folds from regional 2D seismic lines, to investigate the relationship between fold growth, fault propagation and fault interaction across the basin. We show that: (i) normal fault-related folds can be generated by different mechanisms that vary in importance in time and space along a single fault array; (ii) the heterogeneous mechanical properties of the host rocks control the fault segmentation and associated ductile deformation; and (iii) the occurrence and development of normal fault-related folds is influenced not only by mechanical stratigraphy and fault plane geometry, but also by mechanical interaction between the faults themselves. Specifically, the variability of extensional folding along the strike of a fault array can be explained by the enhanced vertical propagation due to mechanical fault interaction between opposite-dipping normal faults.

Geological setting

Regional tectonic framework

The studied fault system is located in the Inner Moray Firth (IMF) basin (*Figure 1*). The basin is characterized by NE-SW striking normal faults that accommodated an Upper Jurassic-Early Cretaceous extensional episode which resulted in the opening of the North Sea rift system (Ziegler, 1990; Thomson and Underhill, 1993; Davies et al, 2001). Some authors

proposed a transtensional opening of the IMF basin (Roberts et al, 1990). We have no evidence for fault oblique displacement, but previous studies considered that faults in the area of interest are dominated by dip-slip displacement (Underhill, 1991; Davies et al, 2001; Long and Imber, 2010) and that any strike-slip movement was associated mainly with Great Glen Fault (to the northwest of the present study-area) and post-dated Mesozoic rifting (Underhill, 1991). Regional, Late Cretaceous post-rift subsidence and sedimentation were followed by Cenozoic uplift and reactivation of some of the faults. These faults show very mild post-Cretaceous reactivation, as indicated by small-scale folding of the Base Cretaceous horizon (H7 on *Figure 1b*), but there is no evidence of large inversion structures affecting the geometries of the pre-inversion folds.

Stratigraphic framework and mechanical stratigraphy

The stratigraphy of the IMF can be divided into pre-, syn- and post-rift tectono-stratigraphic sequences (*Figure 1 and 2*). Our study investigates deformation within the upper part of the Triassic to Early - Middle Jurassic, pre-rift succession (pre-H3 horizons), and within the Late Jurassic, syn-rift succession (H3-H7) (*Figure 2*). We used information from nearby wells and published literature (Stevens, 1991) to infer the presence of three main mechanical units, based on stratigraphic variations in the net-to-gross ratio (*Figure 2*).

Horizon H1, which follows a strong and regionally continuous seismic reflection, corresponds to the top of the mechanical unit 1 (MU 1). Well data indicate that H1 follows the top of the pre-rift, Triassic alluvial plain sandstones of the Lossiehead Formation (> 100 m thick; *Figure 2*). These strata overlie the Permian to Permo-Triassic Hopeman, Bosies Bank and Rotliegend formations, all of which are dominated by sandstone lithologies. In turn, the Permian deposits unconformably succeed the Devonian Old Red Sandstone (Goldsmith et al, 2003; Glennie et al, 2003). Based on the high net-to-gross of the Lossiehead Formation and underlying strata, we infer that MU 1 is likely to be mechanically "competent", here defined as being susceptible to deformation by seismic-scale faulting.

The upper part of the pre-rift sequence (H1-H3 interval; *Figure 2*) comprises a ~300 m thick succession of interbedded sandstones and shales with a net-to-gross ratio of 38%, which we define as mechanical unit 2 (MU 2). We infer that the alternation of competent sandstones and less competent shale layers is likely to favour layer-parallel slip (Watterson et al, 1998). At the time of rifting, these Lower-Middle Jurassic sediments may have not been completely lithified, and were probably characterised by a reduced strength contrast between the

sandstones and weaker shale layers. However, results of discrete element method modelling have shown that deformation can be partitioned between layers with small strength contrast at low confining pressure conditions (Schöpfer et al, 2007), with faults initiating in the slightly more competent sandstone layers. We hypothesise that thicker and relatively stiffer sandstone intervals within the MU 2, such as the 50-60 m thick "H" and "I" reservoir sandstones of the Beatrice Field (Stevens, 1991), may favour fault nucleation and propagation (see section *Spatial and stratigraphic variations in fault throw and fold amplitude*), whilst the intervening shale intervals (e.g. Lady's Walk Shale) may inhibit fault propagation (*Figure 2*). This overall arrangement is likely to promote vertical segmentation of faults.

The syn-rift sequence (H3-H7 mapped horizons) thickens toward the main faults and is dominated by Upper Jurassic shales, which we define as mechanical unit 3 (MU 3). This succession is likely to be mechanically "incompetent", here defined as being susceptible to distributed (i.e. ductile) deformation. Hangingwall reflectors within several hundreds of metres of the mapped faults clearly dip toward the graben (synthetic layer dips *sensu* Ferrill et al, 2005), with hangingwall syncline depocentres shifted away from the fault. Previously, these folds have been interpreted as the result of differential compaction of the shale-dominated syn-rift sequence (MU 3) overlying the older and more rigid pre-rift, footwall formations (MU 1 and 2) (Thomson and Underhill, 1993). While we do not exclude the possibility that some folds are the result of compaction, we show below that the analysed hangingwall folds display structural patterns that cannot be attributed to compaction, and that compaction effects are secondary with respect to other mechanisms.

Dataset and methods

Seismic and well data

The dataset used in this study comprises a 3D reflection seismic survey acquired over the Beatrice Field (Linsley et al, 1980; Stevens, 1991) and several regional 2D seismic lines that are orientated NW-SE, orthogonal to the main structure of the Inner Moray Firth Basin. The 3D time-migrated seismic data covers an area of 11 x 22 km, and has a crossline and inline spacing of 12.5 m. The dominant frequency for the interval of interest is between 30-40 Hz, with velocities ranging between 2500-3500 m/s (*Figure 3a*), resulting in a vertical seismic resolution of 15-30 m. Velocity data from the Beatrice wells indicates a consistently increasing velocity with depth, with no significant lateral or vertical velocity variations (*Figure 3a*). There are no significant variations in geometry between time and depth data, just

a relatively uniform expansion by a factor of 1.55 on the depth profiles (*Figure 3b*). As a result, we used the two-way-time data to measure parameters such as fault throw and the amplitude of the hangingwall folds. However, when we analysed attributes such as fault dip, the fault surfaces have been converted to depth in order to show the realistic geometries of the faults. Eight seismic horizons were mapped in total (seven in detail: H1-H7) within the pre-rift and syn-rift stratigraphic intervals, with Beatrice Field wells providing information on the associated lithological formations. The study focusses on the segmented, SE-dipping ABC fault array (see box in *Figure 1c*), supplemented by examples from other fault systems to highlight salient points.

Methods

We used several methods to analyse the distribution and growth of the faults and folds:

(i) *Throw-distance (T-x) profiles* and *throw-depth (T-z) profiles* enabled us to investigate the lateral and vertical variations in discontinuous fault throw and continuous deformation (folding), and to analyse the lateral and vertical linkage of faults (Walsh and Watterson, 1991; Childs et al, 1996; Mansfield and Cartwright, 1996; Hongxing and Anderson, 2007; Long and Imber, 2010; Tvedt et al, 2013; Jackson and Rotevatn, 2013; Rotevatn and Jackson, 2014). For T-x profiles, fault throw was measured perpendicular to the strike of the fault every 125 m (every 10th inline), with more dense sampling points near the fault tip or where the fault complexity required it;

(ii) *Isochore thickness maps* and *expansion indices* were used to analyse the timing of faulting and folding (Tvedt et al, 2013; Jackson and Rotevatn, 2013) and to constrain the position of the upper tip-line at the time of deformation. The expansion index (Thorsen, 1963) is defined by the ratio between the maximum thickness of a chosen syn-rift interval in the hangingwall of a fault (adjacent to the fault surface, or within the synclinal depocentre) and the thickness of the equivalent interval in the footwall;

(iii) *Fault surface analysis* provided insights into the relations between fault geometry and linkage style, expressed by parameters such as fault dip, fault cylindricity and throw variation (Ziesch et al, 2015), and distribution of ductile deformation. Cylindricity measures the deviation of a fault surface from a best-fit planar surface (Ferrill, 2000; Jones et al, 2009; Ziesch et al, 2015);

(iv) *Seismic trace and coherency attributes* (a combination of instantaneous phase, tensor, discontinuity and semblance attributes) (Chopra and Marfurt, 2005) were used in some cases

to enhance the visibility of deformational patterns at the limit of seismic resolution within the hangingwall folds (Iacopini and Butler, 2011), or to highlight the fold geometry (dip, dip-azimuth) and stratal onlaps onto fold limbs.

Observations of normal faults and fault-related folds from 3D seismic data

Geometric characteristics of the studied faults and fault-related folds

At H1 (Top Triassic) level, the studied fault system comprises three left-stepping normal fault segments named A, B and C. These are separated by two relay zones. The relay ramp between faults A and B is at an early stage of breaching (*Figure 1c*). At the base syn-rift level (H3), the relay ramps are completely breached by the footwall faults, forming a continuous fault trace. Bends in the fault trace are associated with minor, hangingwall splay faults (*Figure 4a*). This downward bifurcation, (with intact or partially breached relay ramps at depth, and breached relay ramps at shallower levels), seems to be a common feature in our area of study (see section *Spatial and stratigraphic variations in fault throw and fold amplitude*).

The seismic sequence between the H3 and H7 horizons thickens toward the analysed faults, consistent with their syn-sedimentary nature. The ABC fault array is part of a larger NE-SW striking normal fault system that dips SE, along with the faults bounding the Beatrice Field structure, here named D, E, F and G. These two major fault systems are linked within the syn-rift sequence (on horizons H6-H7) by smaller segments (segments b and c) that splay upward from the main faults (*Figure 4b* and *4c*). The upper tip-lines of fault C and the SW continuation of fault B (named B2) are buried within the H3-H5 interval, and are overlain by parallel seismic reflections. These observations indicate that the faults become inactive during the later syn-rift stage, when linkage of the AB fault with the D fault occurred. Faults B2 and C are located within a larger syn-rift transfer zone comprising the synthetic dipping D and E faults, but also the opposite (NW) dipping faults H, I and J (*Figure 4a*), with which B2 and C form a conjugate normal fault pair (*Figure 4d*).

At H1 level, we observe that the deepest structural levels lie immediately adjacent to the fault trace (*Figure 1c*), whilst at H3 (base syn-rift) and H6 (intra-syn-rift) levels, the depocentres are shifted further into the hangingwall, with increasing distance from the fault on progressively younger syn-rift horizons (*Figure 4a* and *4b*). At H3 level, the faults are bordered on the hangingwall side by monoclinal folds with limbs that dip in the same

direction as the fault (*Figure 4a* and *4c*). However, not all the faults are associated with folds at horizon H3 level: faults B2 and C appear to have depocentres adjacent to the fault trace (*Figure 4a* and *4d*). Hence, an intriguing question is why do some faults display hangingwall folds and depocentres that are shifted into the hangingwall, whilst others in the same array lack folds and are characterized by depocentres adjacent to the fault trace? The fact that the folds are developed within the *pre-rift* sequence, and that their location does not necessarily correspond with the major depocentres suggests that the generating process cannot be entirely attributed to differential compaction (cf. Thomson and Underhill, 1993).

Seismic attribute analysis using the instantaneous phase attribute shows that folds associated with the B2 fault are associated with clear, antithetic-dipping axial planes that separate the upward-widening monocline from the hangingwall synclines *(Figure 5a* and *5b*). This fold does *not* display vertical axial planes and thinner hangingwall dipping limbs, which are characteristic for compaction folds in the hangingwalls of normal faults (Skuce, 1996). The instantaneous phase attribute also highlights seismic reflections within the syn-rift sequence that onlap onto the steep limb of the monocline. These onlaps are an indication of the fold growth, rather than the effect of compaction. Furthermore, a combined tensor-semblance-discontinuity attribute indicates the presence of secondary faults (steeply dipping normal faults or even small reverse faults) associated with the monocline that, presumably, accommodated folding (*Figure 5c*). These secondary faults resemble the hangingwall deformation structures of normal fault-propagation folds modelled in clay (Withjack, et al 1990), and described in other rift settings which exhibit extensional fault-propagation folds, e.g. Suez Rift, NW Egypt (Sharp et al, 2000; Khalil and McClay, 2002).

Fault dips are commonly observed to be gentler within the syn-rift and late pre-rift sequences (mechanical units 3 and 2) compared with the early pre-rift sequence (MU 1) (e.g. see segments b, e and f in *Figure 4c* and *4d*; and the fault dip attribute map in *Figure 9b*). The change in fault dip therefore corresponds to the change in lithology from the mechanically competent Triassic sandstones (H1 and below), to the Lower-Middle Jurassic interbedded shale-sandstone succession (H1-H3) and Upper Jurassic shales (H3-H7). The overall effect is to generate pronounced convex upward fault geometries (*Figure 4c* and *4d*) but, because the upward transition to gentler fault dips occurs within the *pre-rift* interval, differential compaction should be secondary in respect to other factors. We can explain the difference in dips by the variation in shear failure angles within rocks that have different mechanical properties (Mandl, 1988), with higher angle faults developed within the mechanically

competent Triassic sandstones (MU 1). These observations have important consequences for understanding the vertical segmentation of faults across the different mechanical units, a point we return to in the following section.

Spatial and stratigraphic variations in fault throw and fold amplitude

Figure 6 is a T-x profile showing the variation in throw (i.e. the discontinuous component of vertical displacement) along the strike of faults A, B and C. We observe a systematic decrease in throw towards the SW, with the largest throws within the pre-rift sequence (H1 level) reaching 300 ms (~450 m) along fault A and decreasing to a maximum of ~100 ms (~155m) along fault C. Note that fault A continues beyond the NE limit of the 3D seismic volume. The profiles for faults A and B display distinct throw minima that correlate with undulations in the fault trace, fault surface corrugations and the locations of transverse hangingwall folds (*Figure 1c, Figure 6 and Figure 9a*). These observations suggest that at H1 level, fault A comprises at least three linked fault segments and fault B comprises two linked segments (B1 and B2 in *Figure 1c*). We propose that faults A and B formed through the coalescence of multiple fault segments and that "corrugation zones" mark the locations of former segment boundaries (*Figure 6 and Figure 9a*).

The syn-sedimentary nature of the faults is reflected by a systematic, upward decrease in throw within the syn-rift interval (H3-H7) (*Figures 6 and 7*), and by the horizontal pattern of the throw contours projected onto the fault surface (*Figure 8*) (Childs et al, 2003). Some of the throw-depth (T-z) profiles display an upward decrease in throw within the *pre-rift* interval (between H1 and H2-H3 for profiles P2-P6; *Figure 7*) as a consequence of folding. *Figure 6* shows that the amplitude of folding (measured on H3) approximately compensates for decreases in throw, and varies significantly along the strike of the fault. Folds are not observed adjacent to faults B2 and C, which display throw maxima at H3 level, i.e. at the top of the pre-rift interval (profiles P7-P9, *Figure 7* and *Figure 8*). Another observation that can be made from the T-z profiles is that within the syn-faulting interval, the throw values for H6 and H5 markers are very similar (*Figure 7*), which indicates either that the ~40-50 ms (60-80 m) displacement post-dated deposition of H5-H6, or that the ratio of fault throw rate to sedimentation rate may have decreased during this interval.

Previous studies have shown that bends in a fault plane, such as those described in the previous section, can result from vertical fault segmentation and linkage within an incompetent mechanical unit (Childs et al, 1995). Fault L (*Figure 1c*, *Figure 2* and *Figure*

10) provides a clear example of vertical segmentation across contrasting mechanical units. *Figure 2* and *Figure 10c* show there is a marked upward decrease in the dip of fault L, which corresponds to the lithological boundary between the mechanically competent Triassic sandstones of MU 1 and the interbedded, Early-Middle Jurassic succession of MU 2. This change in dip coincides with a throw minimum that separates two distinct throw maxima within MU 1 and the Middle Jurassic H and I Sands (H2) within MU 2 (*Figure 2* and *Figure 10b*). Based on these observations, we infer that the upper, en-echelon segments La, Lb and Lc (*Figure 10*) probably nucleated within the Middle Jurassic H and I sands, and linked with the deeper L1 and L2 segments within the underlying, incompetent Lady's Walk Shale formation. This vertical linkage generated a convex upward fault geometry, with a pronounced bend developed in the linkage zone (*Figure 2*), expressed by the gentle fault dips and displacement minima (Childs et al, 1995). The fault bend geometry is controlled by the spatial position of the upper segments (e.g. La, Lb and Lc) relative to the location of the deeper main faults (e.g. L1 and L2). Essentially, the fault bend (or fault ramp) is controlled by the separation distance between the vertically segmented normal faults, with the widest ramp corresponding to the largest segment separation. As a consequence, the locations of the bends in the fault plane can be variable along strike of the fault array and explains the observed geometries of the analysed faults (*Figures 9* and *10*). The changes in fault dip correspond, in some cases, with downward-bifurcation of fault segments, in which relay ramps are breached at shallower levels but remain intact at depth (*Figure 10*). These fault patterns, which are similar to the geometry of the faults A and B, are unusual for coherent fault models that describe fault growth by upward-bifurcation (Walsh et al, 2003), suggesting again vertical linkage (Marchal et al, 2003; Jackson and Rotevatn, 2013; Rotevatn and Jackson, 2014) by downward propagation of segments that nucleated within the shallower Jurassic sequence.

The relationship between vertical segmentation and folding is illustrated in *Figure 4c* and *4d*. Here, we observe that segments b, e and f dip gently within the syn-rift section and that the linkage with the deeper main faults varies along strike. Close to its lateral tip (where the displacement is small), fault F is not hard-linked to the overlying segment f. Instead, the two faults are separated by a monocline that overlies the upper tip line of fault F (*Figure 4a, 4b and 4c*). Analogue models indicate that discontinuities within layering (analogous to the heterogeneities in mechanical properties of the MU2 and MU3) tend to promote breaching of the monocline by downward propagation of a fault that nucleates at shallow depths above the

footwall of the main, underlying fault, and which are not initially hard-linked to the main fault (Bonini et al, 2015).

A similar situation is indicated by high reflector dips observed above other fault arrays within the 3D seismic volume. For example, horizon H3 displays high reflector dips above the tip lines of segments La, Lb and Lc (*Figure 10a*, H3 horizon dip map). This observation is consistent with folding ahead of the propagating tip of the "L" segments (Ferrill et al, 2007; Long and Imber, 2010). With increasing displacement, we suggest that the monocline (expressed by high reflector dips at H3 level), is likely to be breached completely and subsequent translation of the hangingwall across the convex upwards fault plane will increase the amplitude of the initial fault propagation fold, possibly completely overprinting it. The final amplitude of the fold will therefore vary along strike as a function of the initial amplitude of fault propagation-fold, the amount of throw, and the geometry of the fault bend.

Summary of key observations and inferences

Mechanical unit 1 is characterised by steeply dipping faults that accommodated localized displacement with little evidence for associated folding. Fault dips are gentler within MU 2 and 3, reflecting the lower shear failure angles associated with these mechanically less competent units, and vertical linkage zones with the main faults. Fault propagation folds overlie the upper and lateral tip lines of faults within MU2 and 3, and we infer that the competence contrast between MU 1 and the overlying strata promoted vertical segmentation and linkage of faults. Contrary to a previous study, several observations suggest that differential compaction is unlikely to have been the primary mechanism responsible for fold generation. We now investigate the fold growth in more detail.

Folding mechanisms

Fault-propagation folding

Isochore thickness maps provide insights not only into the growth of the faults but also on the early growth and development of the fault related folds. *Figure 11* shows the stratigraphic thickness of the early syn-rift interval (H3-H4). Hangingwall syncline depocentres are observed along the strike of faults A and B. *Figure 11b* is a graph of the stratigraphic thickness of the H3-H4 interval measured along strike of the fault in the footwall, in the hangingwall and within the hangingwall syncline. We observe that the maximum recorded thickness is located predominantly within the syncline depocentres. Similar thicknesses in the

footwall and in the proximal part of the hangingwall along parts of A and B suggests that, at the time the H3-H4 sequence was deposited, parts of these faults were blind and overlain by a gentle monocline, with growth strata onlapping the monocline limb (*Figure 11b* and *Figure 10*). At this stage, the amplitude of the monocline reached ~ 40 ms (50-60 m), indicated by the difference in the real stratigraphic thicknesses of the syn-faulting deposits in the syncline and in the proximal part of the hangingwall, with the condition that this latter thickness is similar to the stratigraphic thickness in the footwall (*Figure 11b*). We suggest that vertical propagation of faults A and B was inhibited within the ductile, shale-dominated Early-Middle Jurassic sediments, most likely within the Lady's Walk Shale Formation, considering that horizon H2 is also folded. Other faults from the study area that exhibit vertical segmentation (e.g. faults L, N) display lateral offsets or dip linkage (and associated bends in the fault plane) within the same stratigraphical level.

The formation of a fault propagation fold is controlled by the relative position of the upper tip-line of the faults with respect to the mechanical stratigraphy, in our case, by the presence of MU 2. Our observations show that the elevation of the vertical tip-line was very variable along the strike of the fault ABC, hence a question arises: why in some places was the upper tip line buried beneath the free surface (developing a fault propagation-fold) whilst in other places, for example along the conjugate fault pairs B2-H and C-I, did the fault breach the depositional surface shortly after the onset of rifting? We do not have any evidence from wells, or from the analysis of the seismic facies, of any significant lateral changes in lithology or a decrease in thickness of MU 2, which together could enhance upward propagation of the faults and early surface breaching. Expansion indices show constantly higher values for faults C and B2 for the H3-H4 interval, compared with segment B1 and parts of A (*Figure 11c*). These high expansion indices can be an indicator of the high displacement rates on these two faults during deposition H3-H4, which is consistent with their early breaching of the surface. We propose a mechanical explanation for these observations in the *Discussion* section.

Fault-bend folding

The present-day fold amplitudes on horizon H3 are very variable (stippled line on the T-x profile, *Figure 6*), and larger than the amplitudes inferred to be solely the result of initial fault propagation folding (*Figure 11*). *Figure 9b* shows that the lateral distribution of folds correlates well with the extent of regions characterised by upward decreases in dip of the ABC fault plane. We observe that the fold amplitude is largest where there is a more

pronounced change in the fault dip with depth (adjacent to faults A and B1) (*Figure 6*). The increase in the fold amplitude of H3 also seems to correlate with increasing displacement of the H1 horizon (*Figure 6*). At shallower levels, *Figure 4b* and *4c* show that the H6 horizon developed a broad anticline flanked by a depocentre immediately adjacent to the trace of fault b, and another broad, distal synclinal depocentre parallel with the fault trace. This morphology is similar to the hangingwall geometries developed above ramp-flat-ramp normal faults (McClay and Scott, 1991; Rotevatn and Jackson, 2014). We will come back to discuss the relation between fault-bend and fold amplitude in the following sections.

Analysis of normal faults and fault-related folds from a regional (basin-wide) dataset

2D geometry of faults and fault-related folds

To obtain a more representative sample of the extensional fault-related folds from the IMF basin, we analysed a further 57 cross-sections from the regional 2D seismic dataset in addition to measurements of the 18 faults interpreted from the 3D survey. Examples of the analysed extensional folds are illustrated in *Figure 12*. Most of the faults terminate within the syn-rift sequence and are associated with monoclinal folds above their upper tip points (*Figure 12a* and *12b*). Some of the monoclines are breached by their associated faults, resulting in normal drag-like fold geometries within the hangingwall (*Figure 12e*). The following key observations suggest that the analysed monoclines originated as fault propagation folds: (i) the folds display an upward widening geometry; (ii) there is a qualitative relationship between the amplitude of the monoclines (breached or unbreached) and the amount of throw recorded within the pre-rift sequence; and (iii) in some, but not all cases, reflectors within the syn-rift sequence onlap onto the fold limbs (*Figure 12a*, *12b* and *12c*). Where stratal onlaps are absent, seismic reflectors within the syn-rift sequence have a sub-parallel to slightly divergent pattern away from the fault, with minor differences in thickness between the hangingwall and footwall strata. This observation can be explained by the relatively high sedimentation rates (150-400 m/Myr) in this part of the basin (Davies et al, 2001), which exceeded the relatively low fault displacement rates (Nicol et al, 1997). This interpretation is consistent with the relatively low expansion indices for the H3-H4 interval, compared to the younger analysed intervals (*Figure 11c*). Consistent with our interpretations of the 3D seismic data, breaching of fault propagation folds occurs either by upward propagation of the main faults from below, or by downward propagation of shallower fault

segments that nucleate within the syn-rift sequence (i.e. MU 3), typically within the footwall domain of the monocline (*Figure 12c*, *12e* and *12f*). In the latter case, *v*ertical linkage with the deeper faults may give rise to irregular fault traces.

In summary, our observations and inferences based on the basin-wide, 2D seismic dataset corroborate our initial conclusions based on detailed analysis of the (spatially restricted) 3D seismic dataset, providing confidence in the general applicability of our results. We now undertake a quantitative analysis of fold growth and breaching using the combined results from both datasets.

Quantitative analysis of fold growth and breaching

Our observations show that conjugate faults (e.g. faults B2, C and H, I) tend to breach the depositional surface soon after the onset of rifting. We therefore sub-divide the data into two categories based on the fault geometry. "Simple" normal faults are those *not* associated with a conjugate pair, whilst "conjugate" normal faults are those that interact (and may share a sub-horizontal branch-line) with opposite-dipping faults (*Figure 12* and *13*). Conjugate normal faults may display a cross-sectional V-style geometry if throw is similar on both faults and a Y shape, if displacement is larger on one fault than the other (Nicol et al, 1995). The amplitudes of breached and intact monoclines were measured for two horizons, H3 and H4. Although the data are relatively scattered, we observe that conjugate faults tend to have smaller associated fold amplitudes compared with simple faults (*Figure 13a* and *b*). For example, only 8% of the analysed simple normal faults have no associated folding on horizon H3, compared to 41% of the conjugate faults (*Figure 13a*). 51% of the simple normal faults in our sample are associated with folds that accommodate more than half of the total throw (i.e. ratio of fold amplitude/total throw > 0.5; *Figure 13a*), compared with only 8% of the conjugate faults.

Figure 13 also shows that fold amplitudes vary from 0% to 100% as a proportion of the total displacement (fault throw + fold amplitude) on the two interpreted horizons: H3 (top MU 2) and H4 (intra MU 3). By comparing the ratio of fold amplitude to the total throw on each horizon, we are able to explore the influence of the two different mechanical units on the magnitude of ductile deformation. The extensional fold amplitudes measured for horizon H4 are typically larger than the fold amplitudes of horizon H3 (*Figure 13a and b*). The largest amplitude recorded for an intact monocline (fold amplitude/total throw = 1) for H4 is 120 ms compared with 50 ms for H3. Larger amplitude values observed for breached monoclines

(fold amplitude/total throw < 1) can be explained by increased bed rotation within relay zones (e.g. between vertically segmented faults) and/or by movement of the hangingwall across a bend in the fault surface, which we discuss, below.

Fault-propagation fold geometries (in terms of monocline amplitude and wavelength) can be described by kinematic parameters such as propagation to slip ratio (P/S) and apical angle, which together define the trishear zone of deformation located above propagating blind faults (Hardy and Allmendinger, 2011). P/S ratio, the main controlling factor on the amplitude of the fold, represents the propagation of the fault with respect to the displacement accrued, and is influenced by the mechanical properties of the rocks and the effective confining pressure (Cardozo et al, 2003). Incompetent lithologies tend to inhibit fault propagation by accommodating larger amounts of strain before failure, while more competent layers are characterized by localized brittle shear fractures. The larger fold amplitudes observed on horizon H4 compared to those associated with H3 are consistent with lower P/S ratios associated with propagation of the fault through the shale-dominated H3-H4 interval. This interval, which is part of the syn-rift, mechanical unit 3, has a higher proportion of incompetent shale layers (>90 %) than MU 2 (62%). This observation suggests that fault propagation rates, as a proportion of fault displacement rate, vary according to the ratio of incompetent versus competent lithologies, given that the bulk thickness of the two stratigraphic intervals is similar. The relatively early breaching of the interbedded MU 2 – despite its likely propensity to deform by layer-parallel slip – is consistent with the models of Bonini et al. (2015), which indicate breaching of the monocline by downward propagation of a fault that nucleates at shallow depths above the footwall of the main fault.

As previously shown, vertical linkage may generate a bend in the fault plane that, with increasing displacement, will promote further fold growth as a result of hangingwall translation over the convex upward fault plane. *Figure 13d* shows a series of vectors, plotted in fold amplitude *vs*. total throw space, that illustrate the growth of fault-bend folds on horizon H3 within the 3D seismic survey area. The left-hand point on each vector corresponds to the amplitude of the precursor fault propagation fold (zero in some cases). The right-hand point on each vector corresponds to the final fold amplitude (at the cessation of fault movement) resulting from fault propagation *and* fault-bend folding. According to Groshong (1989), the relationship between fault throw and the amplitude of a fault-bend fold depends primarily on the bend geometry, which is given by the change in fault dip. The maximum throw on the faults presented in *Figure 13d* is similar to the thickness of MU 2,

hence we assume a linear relationship between fault throw and fault-bend folding, since horizon H3 (top of MU2) is not completely displaced over the fault bend. In this situation, steeper gradients (e.g. vectors A and B) correspond with more pronounced bends in the fault surface, while lower gradients (e.g. vector C) are characteristic of more planar faults, which lack or have smaller associated folds (*Figure 13d* and *9*). These observations suggest that the final fold amplitude is the result of both fault propagation and fault-bend folding processes, and that the relative importance of each mechanism may vary significantly along the strike of a single fault array.

Discussion: mechanical interaction between faults and implications for fault propagation and fold development

Geomechanical models indicate that faults interact within the elastic stress fields of neighbouring segments, resulting in asymmetric displacement distributions and preferential locations of slip and/or fault propagation (Willemse et al, 1996; Crider and Pollard, 1998; Maerten et al, 1999). Maerten et al (1999) used boundary element models to analyse the displacement distribution for Y-shape conjugate normal faults within a homogeneous elastic medium, whilst Young (2001) used finite element models to investigate the slip distribution for V-shape conjugate normal faults within a heterogeneous elastic medium (*Figure 14*). Their results showed that conjugate faults are characterized by asymmetric vertical displacement gradients, supporting previous observations from seismic data (Nicol, 1996). They postulated that the asymmetry is unlikely to be the result of nucleation of faults on different layers, but rather is the effect of mechanical interaction between the opposite dipping segments. The models showed that conjugate normal faults display asymmetric displacement distributions that vary with distance between the conjugate segments and the mechanical properties of the material (Young, 2001). *Figure 14c* shows how the Poisson's ratio of the layer containing the fault intersection (i.e. the branch line) influences the fault displacement distribution. The threshold of volumetric strain is lower for less compressible rocks (higher Poisson's ratio) resulting in high horizontal compressive stresses within the fault intersection region. In this case, the mechanical models predict an upward shift of the locus of maximum displacement towards the upper fault tip. This skewed displacement distribution, with higher displacement gradients near the upper tip, implies a greater tendency for preferential upward fault propagation. Specifically, previous studies have shown that the

513 spatial energy release rate, which is a measure of the energy required for a fracture to
514 propagate, is directly proportional to displacement and displacement gradients (Aydin and
515 Schultz, 1990; Willemse and Pollard, 2000).

516 The displacement analysis of simple and conjugate normal faults from the IMF basin shows
517 that the displacement maxima for conjugate normal faults is shifted upwards in the
518 stratigraphic section, to within mechanical unit 2. In contrast, simple normal faults tend to
519 have displacement maxima within MU 1 (e.g. *Figure 6*). The smaller fold amplitude to total
520 throw ratios associated with conjugate faults (*Figure 13*) can therefore be explained by high,
521 upward fault propagation rates due to mechanical interaction between the opposite dipping
522 faults. As a consequence, conjugate normal faults that intersect within layers with low
523 compressibility display geomechanical characteristics favourable for migration of stress
524 concentrations near the upper fault tips. These stress perturbations enhance upward
525 propagation of the fault, generating higher P/S ratios and result in the early breaching of the
526 free surface, and the development of low amplitude extensional folds, or no folding at all.
527 Nevertheless, because some of the conjugate pairs may have formed as a result of incidental
528 intersection of opposite dipping faults (Nicol et al, 1995), it is possible that the faults initially
529 developed as isolated simple normal faults, without mechanical interaction with other faults,
530 at an incipient stage in their evolution. As a consequence, some conjugate faults, typically
531 displaying Y type geometries, may exhibit symmetrical displacement distributions and
532 associated fault propagation folding that is similar to simple normal faults. Further analysis of
533 these faults is required to test this hypothesis.

534 Our findings show that the development of normal fault-propagation folds can vary
535 significantly within a sedimentary basin and will depend not only on the presence of
536 incompetent layers capable of inhibiting fault propagation and causing vertical fault
537 segmentation, but also on the distribution of stress perturbations caused by mechanically
538 interacting normal faults (*Figure 15*). We hypothesise similar relationships should exist
539 between faults and folds in other extensional basins. Seismic data from the Wytch Farm oil
540 field in the Wessex Basin (southern England) reveal similar, vertically segmented normal
541 faults. Displacement maxima are shifted towards the upper fault tips (within the Middle
542 Jurassic Top Cornbrash sandstones) for conjugate faults, compared with the more
543 symmetrical throw distribution for simple normal faults, which have displacement maxima
544 within the Lower Jurassic Bridport and Triassic Sherwood sandstones (see figures 17 and 18
545 E in Kattenhorn and Pollard, 2001). The same mechanism can potentially explain the variable

development of the normal fault propagation-folds seen in other rift settings, such as the Suez Rift, NW Egypt (*Figure 16*, from Whipp, 2011). Here, folds are poorly-developed adjacent to the conjugate West Gordi and East Gordi normal faults. In contrast, large amplitude breached monoclines are developed adjacent to the "simple" Hadahid fault or the rift-border fault (*Figure 16*, from Whipp, 2011). The section in *Figure 16* is overly-simplified, but Whipp (2011) showed that the faults dip at ca. 80° within the basement and overlying Nubian sandstone. In the overlying, interbedded sequence, fault dips decrease to 60-70°, and the faults are vertically segmented. It is likely that translation of the hangingwall monoclines (such as that associated with the Hadahid Fault) across the irregular fault surface contributed to the amplification of the fold amplitude, similar to the example presented from IMF and synthesized in the model shown in *Figure 15*.

Conclusions

Our observations from the Inner Moray Firth basin show that:

(i) The development of a normal fault-related fold can be explained by the contribution of several mechanisms, the relative importance of which change during the growth of the normal fault system. The mechanisms evolve from fault-propagation folding, vertical and horizontal segment linkage to fault bend folding (*Figure 15*).

(ii) The heterogeneous mechanical properties of the host rocks control the fault segmentation and amplitude of fault propagation folding. Shale-rich incompetent layers inhibit fault propagation generating larger amplitude unbreached monoclines. The larger fold amplitudes observed in the shale-rich, syn-rift sequence (mechanical unit 3) compared with the underlying, interbedded pre-rift sequence of similar thickness (mechanical unit 2), demonstrate the importance of the ratio of incompetent to competent strata (net-to-gross ratio) in arresting upward fault propagation and controlling the magnitude of ductile deformation.

(iii) The occurrence and development of the normal fault-related folds is influenced not only by the mechanical stratigraphy and fault geometry, but also by the mechanical interaction between fault segments of a normal fault system. Although incompetent stratigraphic units, dominated by weak lithologies can inhibit vertical propagation of the faults, generating vertical segmentation or development of monoclines above the fault vertical tip-lines, we showed that some faults can breach the free surface very early without developing fault-tip monoclines. The variability of normal fault-related folding can be

explained by the enhanced vertical propagation due to mechanical interactions between opposite dipping normal faults.

We are grateful to Ithaca Energy and Dave Brett for releasing proprietary seismic data for publication. We are thankful to Badley Geoscience Ltd. and Dave Quinn for providing license and training for TrapTester software. We also thank Schlumberger for providing academic license for Petrel, Midland Valley for providing license for Move software and Foster Findlay Associates Ltd. for providing access to GeoTeric software. We thank Al Lacazette, Paul Whipp and Scott Young for the permission to use their figures in this paper. Jonathan Imber acknowledges a Royal Society Industry Fellowship with Badley Geoscience Ltd. and Geospatial Research Ltd. Christopher Jackson, Douglas Paton and Tom Manzocchi provided constructive reviews that significantly improved the clarity of the manuscript.

References

Aydin, A. & Schultz, R.A., 1990. Effect of mechanical interaction on the development of strike-slip faults with echelon patterns. *Journal of Structural Geology* 12, 123-129.

Bonini, L, Basili, R., Toscani, G., Burrato, P., Seno, S., Valensise, G., 2015. *Journal of Structural Geology* 74, 148-158.

Cardozo, N., Bhalla, K., Zehnder, A.T., Allmendinger, R.W., 2003. Mechanical models of fault propagation folds and comparison to the trishear kinematic model. *Journal of Structural Geology* 25, 1-18.

Childs, C., Nicol, A., Walsh, J.J., Watterson, J., 1996. Growth of vertically segmented normal faults. *Journal of Structural Geology* 18, 1839-1397.

Childs, C., Nicol, A., Walsh, J.J., Watterson, J., 2003. The growth and propagation of synsedimentary faults. *Journal of Structural Geology* 25, 633-648.

Childs, C., Manzocchi, A., Nicol, A., Walsh, J.J., Conneally, J.C.,Delogkos, E., *in press*. The relationship between normal drag, relay ramp aspect ratio and fault zone structure. *The Geometry and Growth of Normal Faults, Geological Society of London Special Publication.*

607 Chopra, S. and Marfurt, K.J., 2007. Seismic attributes for prospect identification and
608 reservoir characterization. Geophysical Developments Series. SEG/EAGE Publisher, pp.
609 481.

610 Corfield, S., Sharp, I.R., 2000. Structural style and stratigraphic architecture of fault
611 propagation folding in extensional settings: a seismic example from the Smørbukk area,
612 Halten Terrace, Mid-Norway. *Basin Research* 12, 329–341.

613 Cowie, P.A., 1998. A healing-reloading feedback control on the growth rate of seismogenic
614 faults. *Journal of Structural Geology* 20, 8, 1075-1087.

615 Crider, J.G., Pollard, D.D., 1998. Fault linkage: three-dimensional mechanical interaction
616 between echelon normal faults. *Journal of Geophysical Research* 103, 24,373–391.

617 Davies R.J., Turner J.D., Underhill, J.R., 2001. Sequential dip-slip movement during rifting:
618 a new model for the evolution of the Jurassic trilete North Sea rift system. *Petroleum*
619 *Geoscience*, 7, 371-388.
620 Davis, G.H., 1984. Structural Geology of Rocks and Regions. *John Wiley & Sons, New York.*
621 492 pp.

622 Dula, W.D., 1991. Geometric models of listric normal faults and rollover folds. *American*
623 *Association of Petroleum Geologists Bulletin* 75, 10, 1609-1625.

624 Ferrill, D. A., Stamatakos, J. A., Sims, D., 1999. Normal fault corrugation: implications for
625 growth and seismicity of active normal faults. *Journal of Structural Geology* 21, 1027–
626 1038.
627 Ferrill, D.A., Morris, A.P., Sims,D. W., Waiting, D. J., Hasegawa, S. 2005. Development of
628 synthetic layer dip adjacent to normal faults, *In: Sorkhabi, R. and Tsuji, Y. (Eds.) Faults,*
629 *fluid flow, and petroleum traps. American Association of Petroleum Geologists Memoir*
630 85, 125– 138.
631 Ferrill, D.A., Morris, A.P., Smart, K.J., 2007. Stratigraphic control on extensional fault
632 propagation folding: Big Brushy Canyon Monocline, Sierra Del Carmen, Texas. *In: Jolley,*
633 *S.J., Barr, D., Walsh, J.J., Knipe, R.J. (Eds.). Structurally complex reservoirs. Geological*
634 *Society of London Special Publication,* 292, 203–217.

635 Ferrill, D.A. and Morris, A.P., 2008. Fault zone deformation controlled by mechanical
636 stratigraphy, Balcones fault system, Texas. *American Association of Petroleum Geologists*
637 *Bulletin* 92, 359-380.

638 Ferrill, D.A., Morris, A.P., McGinnis, R.N., 2012. Extensional fault-propagation folding in
639 mechanically layered rocks: The case against the frictional drag mechanism.
640 *Tectonophysics*, 576-577, 78-85.

641 Fossen, H. and Hesthammer,J., 1998. Structural geology of the Gullfaks Field, northern
642 North Sea. *In Coward, M.P., Daltban, T.S. and Johnson, H. (Eds.) Structural Geology in*
643 *Reservoir Characterization. Geological Society of London, Special Publications,* 127,
644 231-261.

645 Fossen, H. 2011. Structural Geology. Cambridge University Press, 463 pp.

646 Glennie, K., Higham, J., Stemmerik, L., 2003. Permian. 91-103. *In: Evans, D., Graham, C.,*
647 *Armour, A. and Bathurst, P. (Eds.) The Millenium Atlas: Petroleum geology of the Central*
648 *and Northern North Sea.* The Geological Society of London.

649 Goldsmith, P.J., Hudson, G., Van Veen, P., 2003. Triassic. 105-27. *In: Evans, D., Graham,*
650 *C., Armour, A. and Bathurst, P. (Eds.) The Millenium Atlas: Petroleum geology of the*
651 *Central and Northern North Sea.* The Geological Society of London.

652 Groshong, R.H., 1989. Half-graben structures: Balanced models of extensional fault-bend
653 folds. *Geological Society of America Bulletin*, 101, 1, 96-105.

654 Gupta, A. and Scholz, C.H., 1998. A model of normal fault interaction based on observation
655 and theory. *Journal of Structural Geology* 22, 865–879

656 Gupta, A., and Scholz, C.H., 2000. A model of normal fault interaction based on observations
657 and theory. *Journal of Structural Geology* 22, 865-879.

658 Hardy, S. and McClay, K.R., 1999. Kinematic modeling of extensional fault propagation
659 folding. *Journal of Structural Geology* 21, 695–702.

660 Hardy, S. and Allmendinger, R., 2011. Trishear. A review of kinematics, mechanics, and
661 applications. *In K. McClay, J. Shaaw and J. Suppe, (Eds.) Thrust fault-related folding.*
662 *American Association of Petroleum Geologists Memoir* 94, 95-119.

663 Hongxing, G. and Anderson, J.K., 2007. Fault throw profile and kinematics of normal fault:
664 conceptual models and geologic examples. *Geological Journal of China Universities* 13,
665 1, 75-88.

666 Iacopini, D. and Butler, R.W.H., 2011 Imaging deformation in submarine thrust belts using
667 seismic attributes. *Earth and Planetary Science Letters*, 302, 414-422.

668 Jackson, C.A-L., Gawthorpe, R.L., Sharp, I.R., 2006. Style and sequence of deformation
669 during extensional fault-propagation folding: examples from the Hammam Faraun and El-
670 Qaa fault blocks, Suez Rift, Egypt. *Journal of Structural Geology* 28, 519-535.

671 Jackson, C.A-L. and Rotevatn, A., 2013. 3D seismic analysis of the structure and evolution of
672 a salt-influenced normal fault zone: A test of competing fault growth models. *Journal of*
673 *Structural Geology* 54, 215–234.

674 Janecke, S.U., Vandenburg, C.J., Blankenau, J.J., 1998. Geometry, mechanisms and
675 significance of extensional folds from examples in the Rocky Mountain Basin and Range
676 province, U.S.A. *Journal of Structural Geology* 20, 841–856.

677 Jin, G. and Groshong Jr., R.H., 2006. Trishear kinematic modeling of extensional fault
678 propagation folding. *Journal of Structural Geology* 28, 170–183.

679 Johnson, K.M. and Johnson, A.M., 2002. Mechanical models of trishear-like folds. *Journal of*
680 *Structural Geology*, 25, 1-18.

681 Jones, R.R., Kokkalas, S. McCaffrey, K.J.W., 2009. Quantitative analysis and visualisation of
682 nonplanar fault surfaces using terrestrial laser scanning (LIDAR) – The Arkitsa fault,
683 central Greece, as a case study. *Geosphere*, 5, (6), 465-482.

684 Kattenhorn, S.A. and Pollard, D.D., 2001. Integrating 3-D seismic data, field analogues and
685 mechanical models in the analysis of segmented normal faults in the Wytch Farm oil field,
686 southern England, United Kingdom. *American Association of Petroleum Geologists*
687 *Bulletin*, 85, 7, 1183-1210.

688 Khalil, S.M. and McClay, K.R., 2002. Extensional fault-related folding, northwestern Red
689 Sea, Egypt. *Journal of Structural Geology* 24, 743-762.

690 Lacazette, A., 2001. Extensional fault bend folding: implications for localized fracturing.
691 www.naturalfractures.com/1.2.3.htm.

692 Lewis, M.M., Jackson, C.A.-L., Gawthorpe, R.L., 2103. Salt-influenced normal fault growth
693 and forced folding: The Stavanger Fault Systen, North Sea. *Journal of Structural Geology*
694 54, 156-173.
695 Linsley, P.N., Potter, H.C., McNab, G., Racher, D., 1980. The Beatrice Field, Inner Moray
696 Firth, UK North Sea. In: *Halbouty, M.T. (Ed.) Giant Oil and Gas Fields of the decade*
697 *1968-1978. American Association of Petroleum Geologists Memoir* 30, 117-129.
698 Long, J.J. and Imber, J., 2010. Geometrically coherent continuous deformation in the volume
699 surrounding a seismically imaged normal fault-array. *Journal of Structural Geology* 32, 2,
700 222-234.

701 Maerten, L., Willemse, E.J.M., Pollard, D.D., Rawnsley, K., 1999. Slip distributions on
702 intersecting normal faults. *Journal of Structural Geology* 21, 259–271

703 Mandl, G., 1988. Mechanics of Tectonic Faulting. Elsevier, New York.

704 Mansfield, C.S., Cartwright, J.A., 1996. High resolution fault displacement mapping from
705 three-dimensional seismic data: evidence for dip linkage during fault growth. *Journal of*
706 *Structural Geology* 18, 249-263.
707 Marchal, D., Guiraud, M., Rives, T., 2003. Geometric and morphologic evolution of normal
708 fault planes and traces from 2D to 4D data. *Journal of Structural Geology* 25, 135-158.
709 McClay K.R. and Scott, A.D., 1991 Experimental models of hangingwall deformation in
710 ramp–flat listric extensional fault systems. T*ectonophysics*, 188, 85–96
711 Nicol, A., Walsh, J. J., Watterson, J., Bretan, P. G., 1995. Three-dimensional geometry and
712 growth of conjugate normal faults: *Journal of Structural Geology* 17, 847–862
713 Nicol, A., Walsh, J.J., Watterson, J., Underhill, J.R., 1997. Displacement rates of normal
714 faults. *Nature*, 390, 157-159.
715 Roberts, A.M., Badley, M.E., Price, J.D., Huck, W., 1990. The structural history of a
716 transtensional basin: Inner Moray Firth, NE Scotland. *Journal of Geological Society*, 147,
717 87-103.
718 Rotevatn, A. and Jackson, C.A-L. 2014. 3D structure and evolution of folds during normal
719 fault dip linkage. *Journal of Geological Society*, 171, 821-829.

720 Rykkelid, E., Fossen, H., 2002. Layer rotation around vertical fault overlap zones:
721 observations from seismic data, field examples, and physical experiments. *Marine and*
722 *Petroleum Geology*, 19, 181-192.

723 Saltzer, D. and Pollard, D.D. 1992. Distinct element modelling of structures formed in
724 sedimentary overburden by extensional reactivation of basement normal faults. *Tectonics*,
725 11, 165-174.
726 Schlische, R.W. 1995. Geometry and origin of fault-related folds in extensional settings.
727 *American Association of Petroleum Geologists Bulletin* 79, 1661-1678.

728 Schöpfer, M.P.J., Childs, C., Walsh, J.J. 2007. Two-dimensional distinct element modeling of
729 the structure and growth of normal faults in multilayer sequences: 2. Impact of confining
730 pressure and strength contrast on fault zone geometry and growth. *Journal of Geophysical*
731 *Research*, 112, B10404.

732 Sharp, I, Gawthorpe, R., Underhill, J., Gupta, S. 2000. Fault-propagation folding in
733 extensional settings: examples of structural style and synrift sedimentary response from
734 the Suez rift, Sinai, Egypt. *Geological Society of America Bulletin*, 112, 12, 1877-1899.

735 Skuce, A.G.1996. Forward modelling of compaction above normal faults: an example from
736 the Sirte Basin, Libya. *Geological Society of London Special Publications*, 99, 135-146.

737 Stevens, V., 1991. The Beatrice Field, Block 11/30a, UK North Sea. *In Abbots, I.L. (Ed)*
738 *United Kingdom Oil and Gas Fields, Geological Society of London, Memoirs*, 14, 245-
739 252.
740 Tavani, S and Granado, P., 2015. Along-strike evolution of folding, stretching and breaching
741 of supra-salt strata in the Platforma Burgalesa extensional forced fold system (northern
742 Spain). *Basin Research* 27, 573-585.
743 Thomson, K. and Underhill, J.R., 1993. Controls on the development and evolution of
744 structural styles in the Inner Moray Firth Basin. *In: Parker, J.R. (Ed.), Petroleum Geology*
745 *of Northwest Europe: Proceedings of the fourth Conference. The Geological Society of*
746 *London*, pp. 1167–1178
747 Thorsen, C.E., 1963. Age of growth faulting in southeast Louisiana. *Gulf Coast Association*
748 *of Geological Societies* 13, 103-110.
749 Tvedt, A.B.M., Rotevatn, A., Jackson, C.A-L., Fossen, H., Gawthorpe, R.L., 2013. Growth of
750 normal faults in multilayer sequences: A 3D seismic case study from the Egersund Basin,
751 Norwegian North Sea. *Journal of Structural Geology* 55, 1-20.
752 Underhill, J.R., 1991. Implications of Mesozoic-Recent basin development in the western
753 Inner Moray Firth, UK. *Marine and Petroleum Geology*, 8 (3), 359–369.

754 Walsh, J.J. and Watterson, J., 1987. Distributions of cumulative displacement and seismic
755 slip on a single normal fault surface. *Journal of Structural Geology* 9, 1039-1046.
756 Walsh, J.J. and Watterson, J., 1991. Geometric and kinematic coherence and scale effects in
757 normal fault systems. *In: Geological Society of London, Special Publications*, 56, 193-
758 203.
759 Walsh, J.J., Childs, C., Imber, J., Manzocchi, T., Watterson, J., Nell, P.A.R., 2003. Strain
760 localisation and population changes during fault system growth within the Inner Moray
761 Firth, Northern North Sea. *Journal of Structural Geology* 25, 307-315.
762 Watterson, J., Nicol, A., Walsh, J.J, Meier, D., 1998. Strains at the intersection of
763 synchronous conjugate normal faults. *Journal of Structural Geology*, 20, 363-370.
764 Watterson, J., Childs, C., Walsh, J.J., 1998. Widening of fault zones by erosion of asperities
765 formed by bed-parallel slip. *Geology* 26, 71-74.
766 Whipp, P.S. 2011. Fault-propagation folding and the growth of normal faults. *Unpublished*
767 *Thesis, Imperial College London,* 518 p.

768 White, I.R. and Crider, J.G., 2006. Extensional fault-propagation folds: mechanical models
769 and observations from the Modoc Plateau, northern California. *Journal of Structural*
770 *Geology*, 28, 1352-1370.

771 Willemse, E.J.M., Pollard, D.D., Aydin, A., 1996. Three-dimensional analyses of slip
772 distributions on normal fault arrays with consequences for fault scaling. *Journal of*
773 *Structural Geology* 18, 295–309.

774 Willemse, E.J.M. and Pollard, D.D. 2000., Normal fault growth: Evolution of tipline shapes
775 and slip distribution. *In: Lehner, F.K. and Urai J.L (Eds.) Aspects of tectonic faulting*.
776 Springer, 193-226.
777 Withjack, M.O., Olson, J., Peterson, E., 1990. Experimental models of extensional forced
778 folds. *American Association of Petroleum Geologists Bulletin* 74 (7), 1038–1054.
779 Withjack, M.O. and Callaway, S., 2000. Active normal faulting beneath a salt layer: an
780 experimental study of deformation patterns in the cover sequence. *American Association*
781 *of Petroleum Geologists Bulletin,* 84, 627-651.
782 Xiao, H. and Suppe, J., 1992. Origin of rollovers. *American Association of Petroleum*
783 *Geologists Bulletin* 76, 509-529.

784 Young, S.S., 2001. Geometry and mechanics of normal faults with emphasis on 3D seismic
785 data, conjugate faults, and the effects of sedimentary layering. *Unpublished Thesis.*
786 *Stanford University*, 167 p.

787 Ziegler, P.A., 1990. Geological atlas of Western and Central Europe. Shell Internationale
788 Petroleum Maatschappij, 554 p.

789 Ziesch, J., Aruffo, C.M., Tanner, D.C., Beilecke, T., Dance, T., Henk, A., Weber, B.,
790 Tenthorey, E., Lippman, A. and Krawczyk, C.M. 2015. Geological structure and
791 kinematics of normal faults in the Otway Basin, Australia, based on quantitative analysis
792 of 3-D seismic reflection data. *Basin Research*, 1-20.

Figures

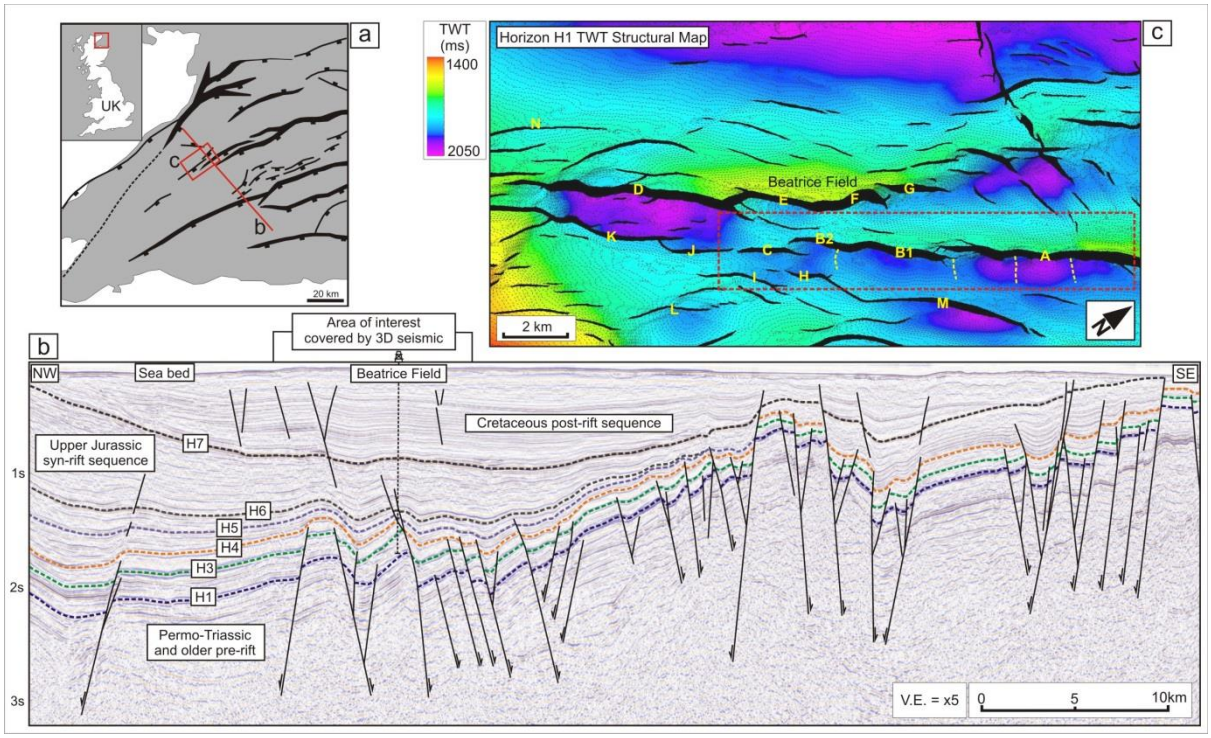

Figure 1 a. Schematic structural map of Inner Moray Firth (IMF) basin (modified from Long and Imber, 2010). **b.** Regional 2D seismic section across IMF, showing the main interpreted horizons and faults. **c.** TWT structural map of pre-rift horizon H1 (Top Triassic). The letters represent the names of the analysed normal faults from the 3D seismic data. The red rectangle delineates the detailed area of analysis. The yellow stippled lines mark the transvere fold hinges separating the depocenters associated with faults A and B.

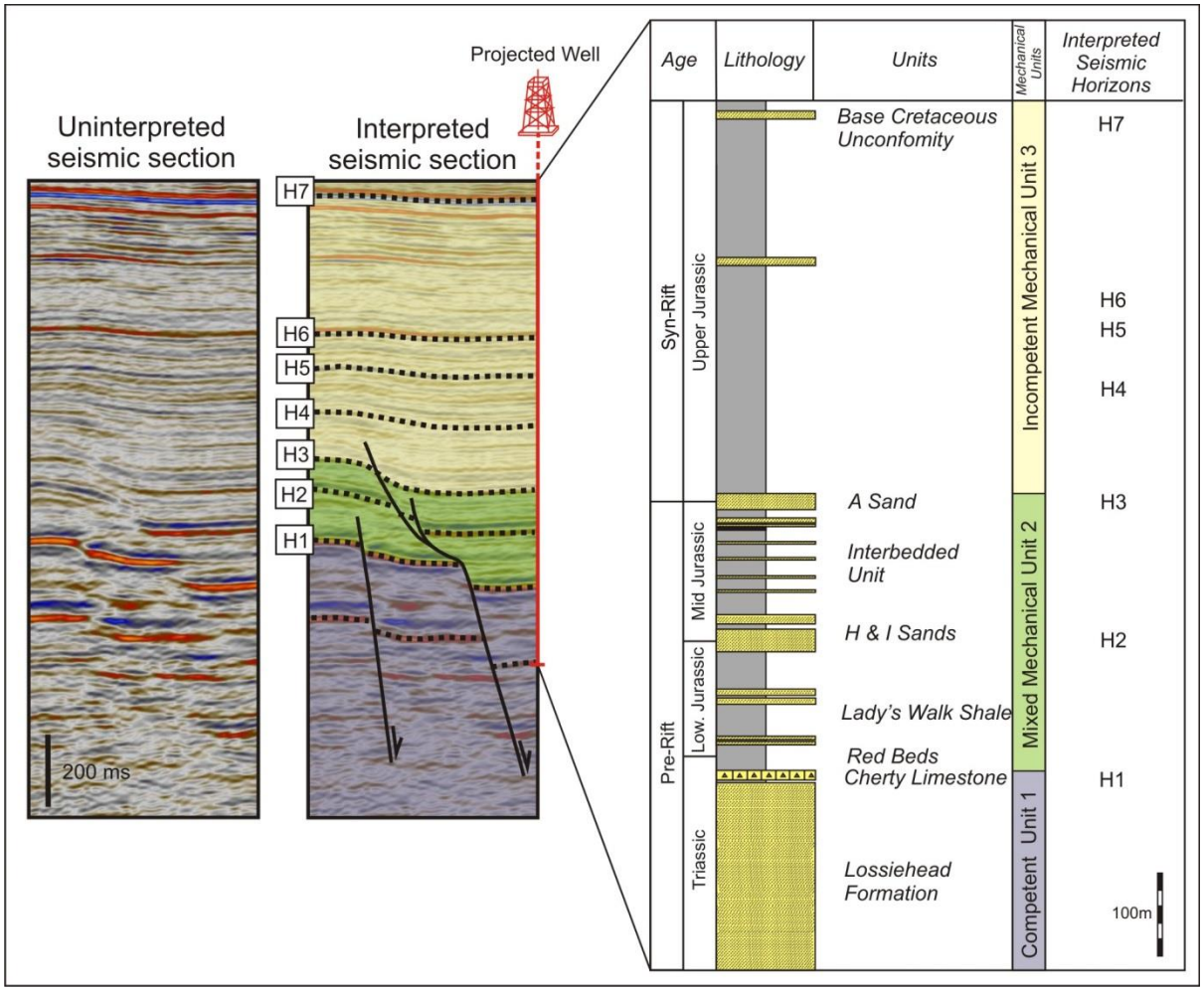

Figure 2. Uninterpreted and interpreted seismic section (with 2x vertical exaggeration) from the studied 3D volume. The mapped horizons and the main mechanical stratigraphic units are shown in the interpreted version. Lithological formations were separated into three mechanical stratigraphic units based on the net-to-gross ratios obtained from the Beatrice Field well data.

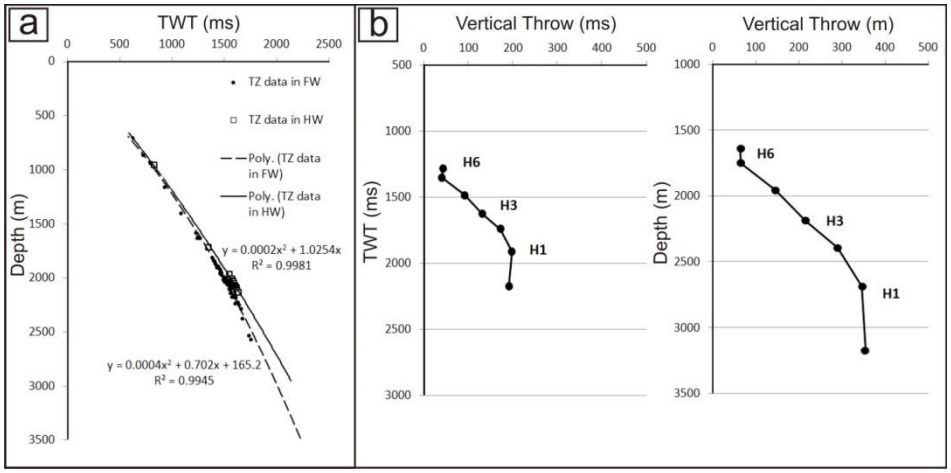

Figure 3 a. Time-depth (T-Z) curves from the Beatrice Field wells showing different velocity gradients for wells which penetrated the footwall or the hangingwall sections of the faults. For depth conversion, we used the T-Z relationship derived from the wells which penetrated the thicker syn-faulting sequences deposited within fault-controlled depocenters because we are interested in quantifying deformation located mainly within the hangingwalls of the faults. This younger, syn-faulting section is characterized by slightly lower velocities compared with the older pre-rift sequence in the footwall. **b.** Comparison of throw distribution in time (ms) with throw distribution in depth (m). The pattern of throw distribution is very similar, but the throw-depth plot shows a vertical expansion of ~1.55.

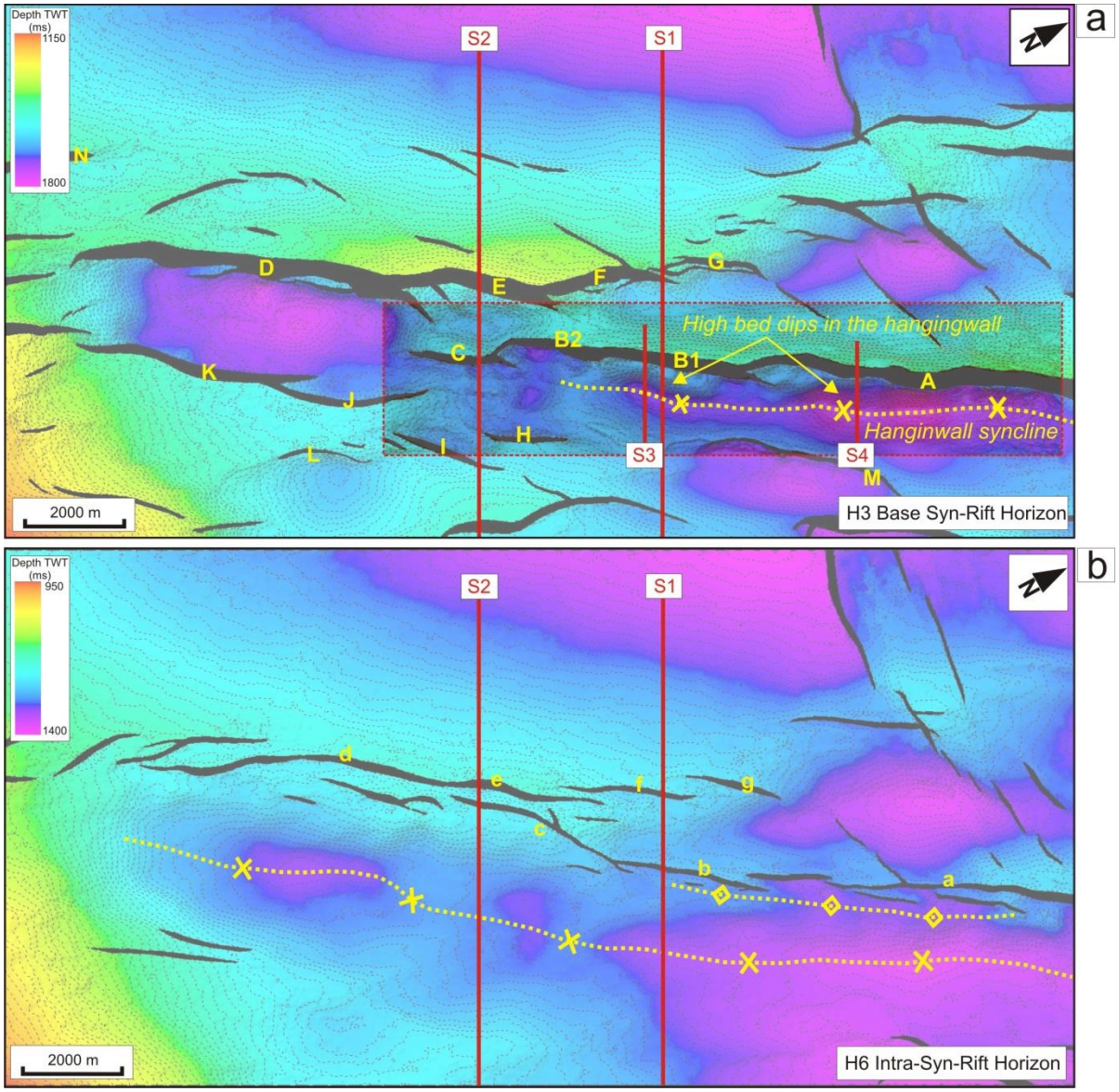

Figure 4 a. TWT structural map of horizon H3 (top pre-rift and top mechanical unit 2); the letters represent the names of the analysed normal faults from the 3D seismic data. The red rectangle borders the A, B and C faults which are analysed in detail. The traces of the faults A and B are bordered by longitudinal folds on the hangingwall side. The steepest reflector dips occur on the fold limb adjacent to the fault traces and are consistently down towards the basin. **b.** TWT structural map of horizon H6 (intra syn-rift). Note the basinward migration of the hinge line of the hangingwall syncline and the decrease in the density of the faults compared with the fault density within the pre-rift sequence (see Figure 1c or 4a).

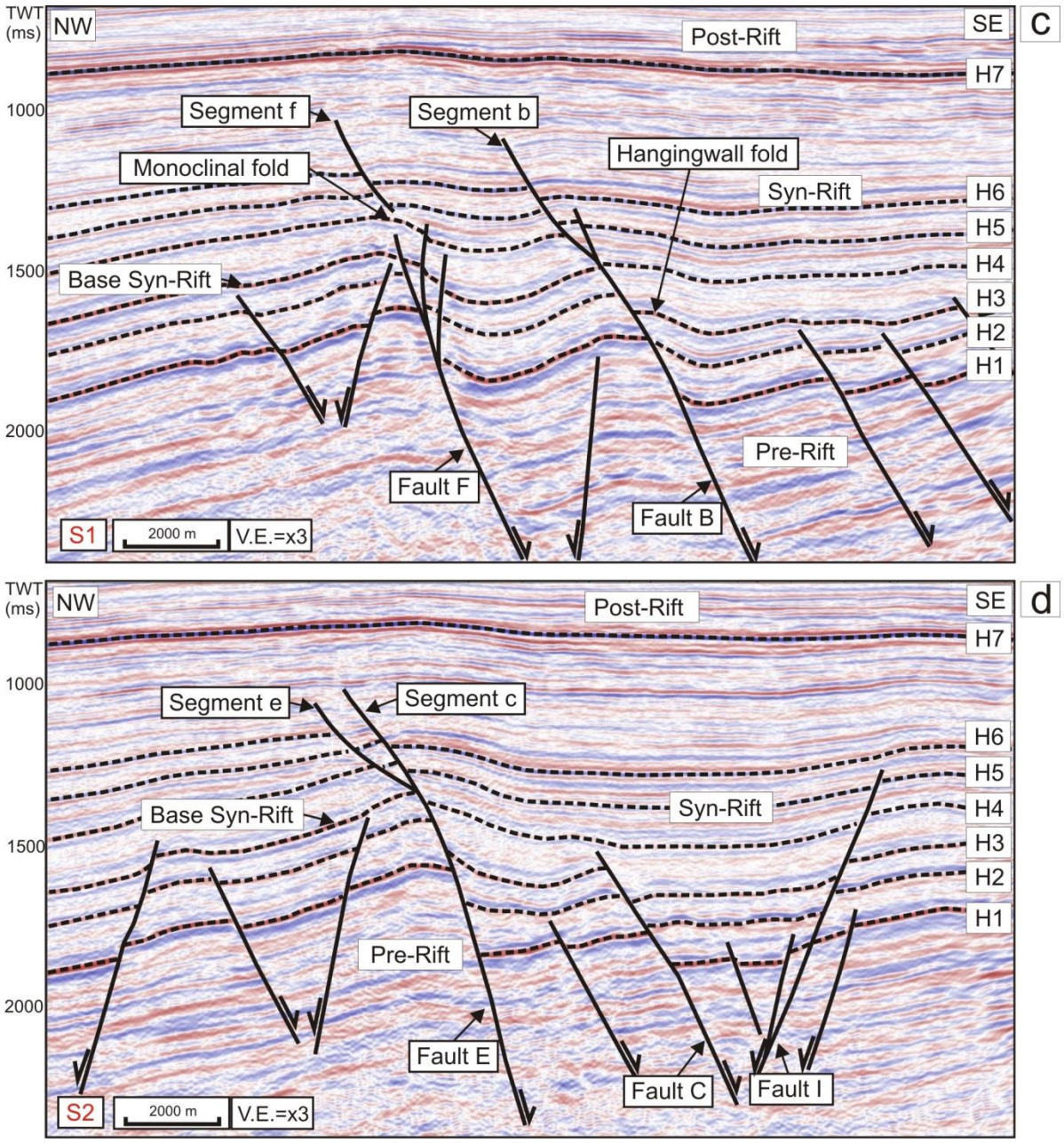

Figure 4 c. and **d.** Interpreted seismic profiles orthogonal to the studied faults. Location in Figure 4a and b (see text for detailed description).

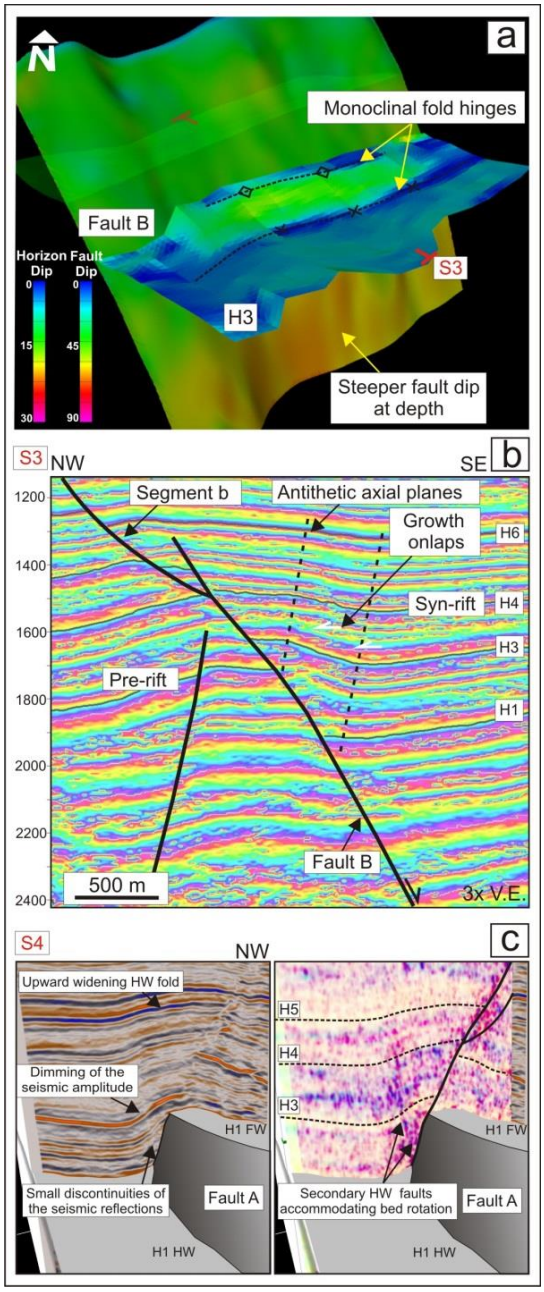

Figure 5 a. 3D view of the breached monocline along Fault B; **b.** Section (S3) displaying the instantaneous phase attribute and showing the breached monoclines associated with Fault B. The instantaneous phase attribute enhances visualization of the reflector configuration, and highlights the onlap of reflectors onto the limb of the monoclinal fold. **c.** Hangingwall fold associated with Fault A (location in Figure 4a) with combined tensor-semblance-discontinuity attribute volume (right) that enhances visualization of secondary faults within the hangingwall of Fault A.

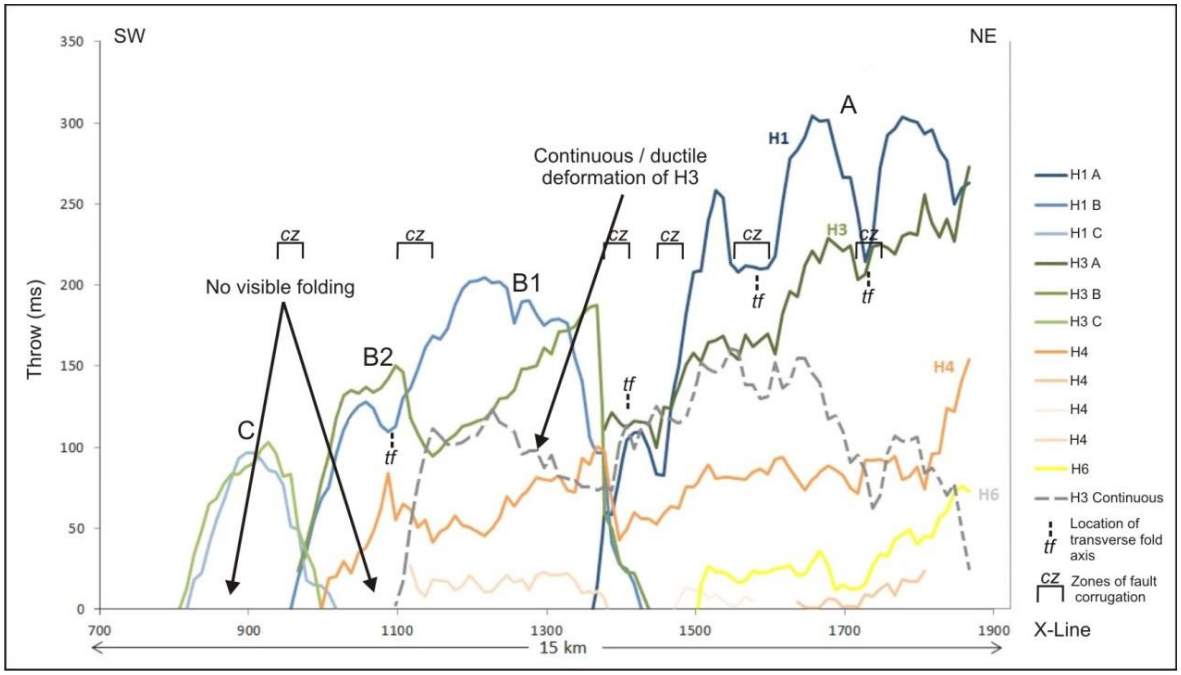

Figure 6. Throw-distance profiles for the 3 analysed fault segments A, B and C (located in Figure 4a). The throw decreases systematically from NE (right) to SW (left), and from the pre-rift (H1) to syn-rift horizons (H3-H6 horizons). The component of ductile deformation (folding) on the H3 horizon was measured separately (stippled line).

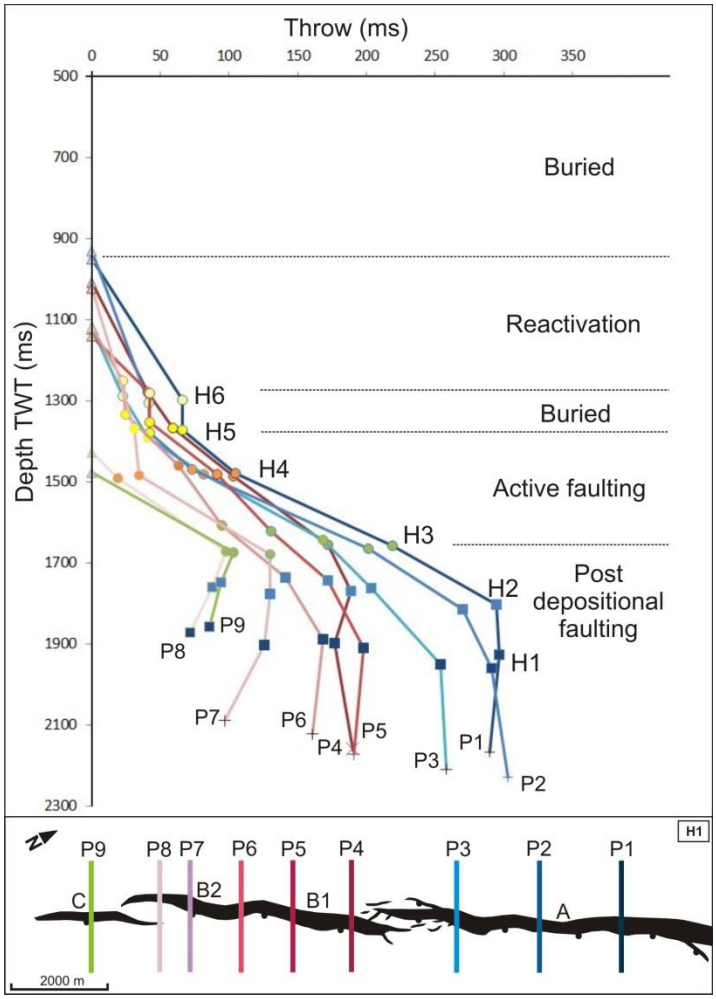

Figure 7. Throw-depth (ms) plots for 9 profiles across the studied faults. The maximum throw is located within the pre-rift section (pre-H3) but varies along the strike of the fault array. The SW part of the B segment and C segment (P7-P9) are characterised by throw maxima at the base syn-rift level (H3). For the other profiles, the lower throw values at base syn-rift are the result of folding.

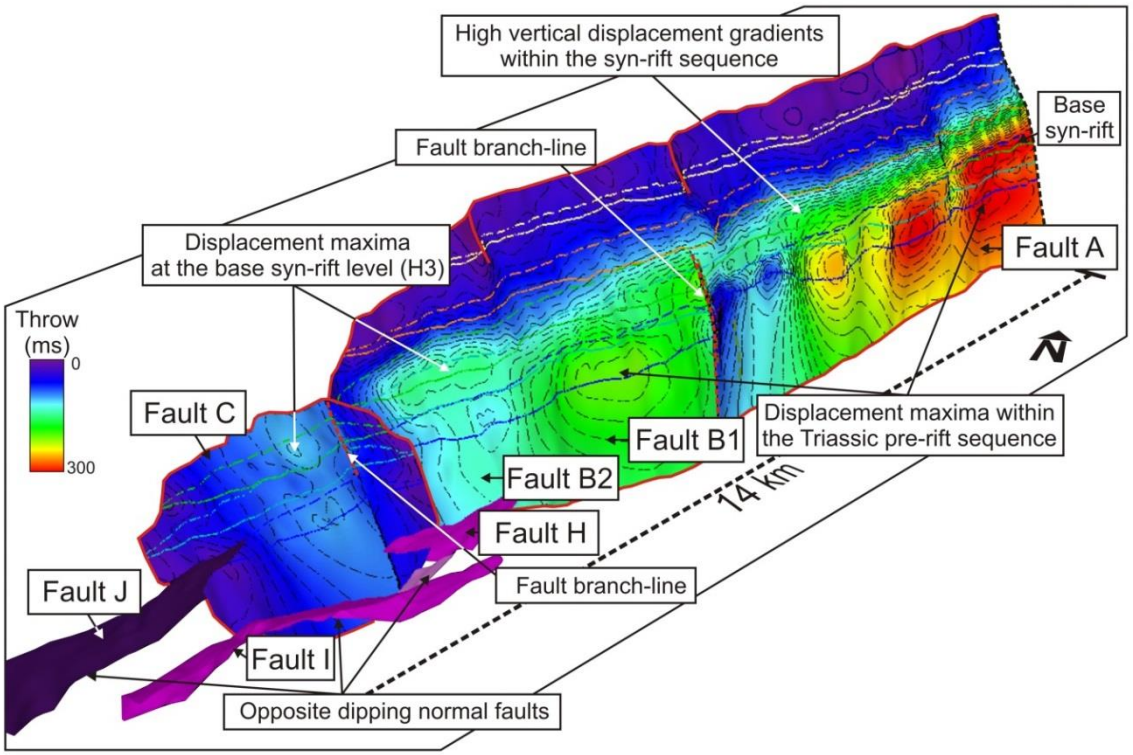

Figure 8. Throw distribution on the A, B and C faults, with horizon cut-offs projected onto the fault surface (continuous line for hangingwall cut-offs and discontinuous line for footwall cut-offs). Note that the maximum displacement is located within the pre-rift sequence for the A and B1 faults. For faults B2 and C, the maximum displacement is shifted upwards towards the base syn-rift.

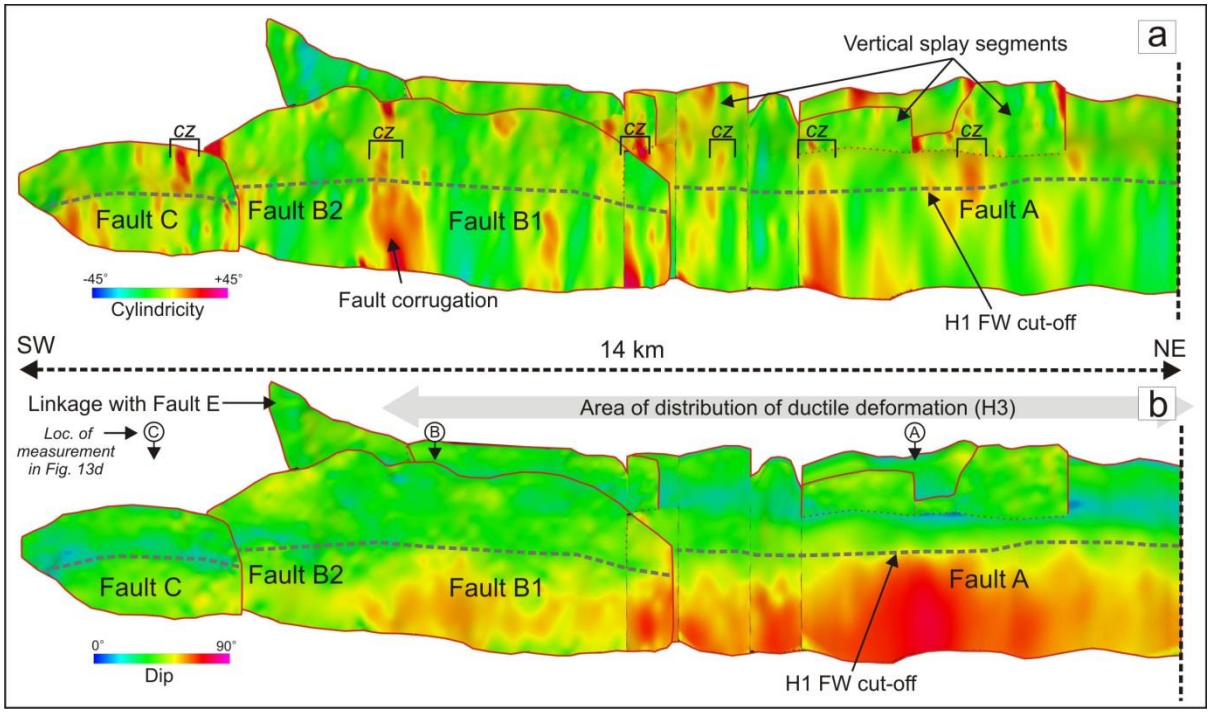

Figure 9. Strike projections of the analysed fault surfaces displaying: **a.** fault cylindricity attribute indicating possible zones of lateral corrugation (cz); **b.** fault dip – note the sharp decrease in fault dip above horizon H1. This change in dip corresponds with a change in lithology, from the Triassic sandstone (mechanical unit 1) to Jurassic shale-sandstone interbedded sequence (mechanical unit 2; see Figure 2).

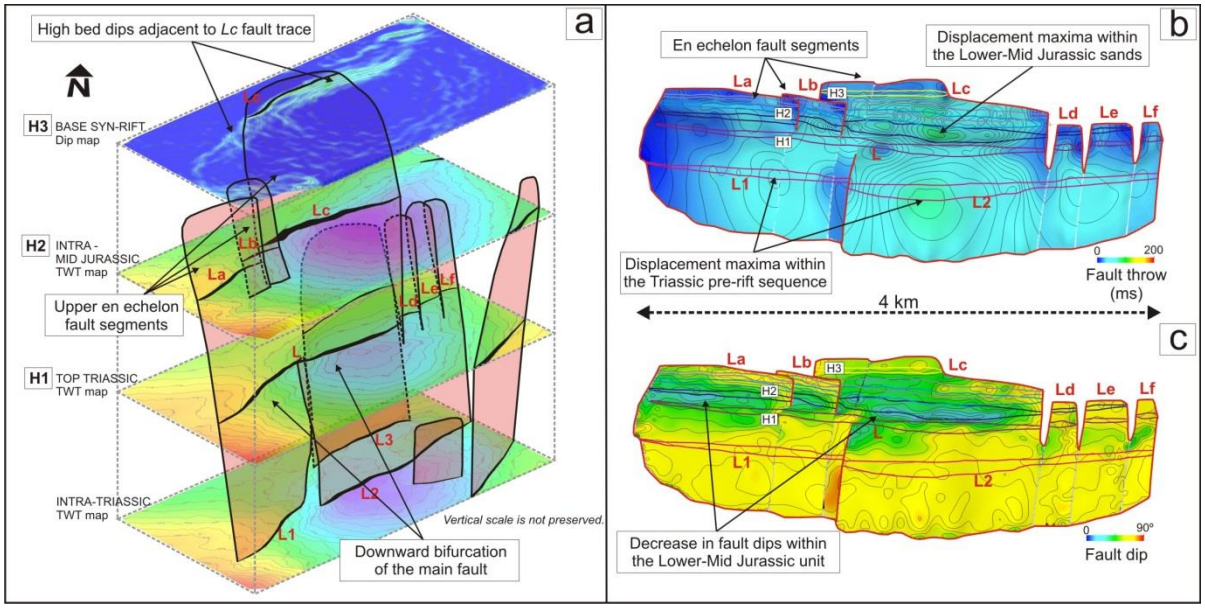

Figure 10 a. 3D diagram showing segmentation of Fault L (location in Figure 1c and 5a) and the main interpreted horizon surfaces adjacent to the fault. Fault-related deformation is characterised by the high bed dips associated with the uppermost surface (H3) in the vicinity of the fault trace *Lc* and above the adjacent blind segments. **b.** Strike projection of Fault L contoured for throw. **c.** Strike projection of Fault L contoured for dip.

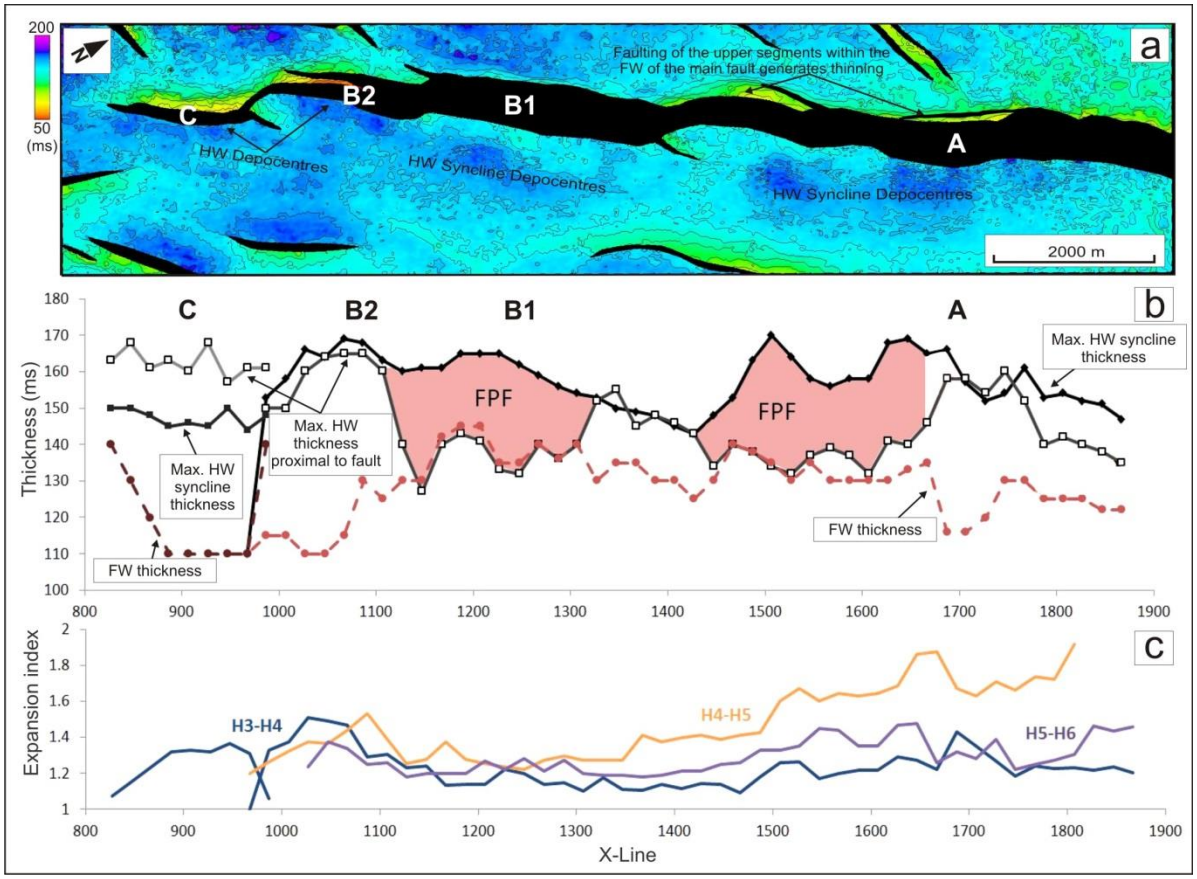

Figure 11 a. Isochore thickness map of the H3-H4 early syn-rift sequence. **b.** Graph with the thickness of the H3-H4 growth sequence measured in the immediate vicinity of the fault trace, in the footwall (dashed red line), in the hangingwall (light black line) and in the hangingwall syncline (bold black line). The fault propagation folds (FPF) are identified where maximum thicknesses are recorded within the hangingwall syncline, and the thicknesses of syn-rift strata within the footwall and proximal part of the hangingwall are similar. **c**. Expansion indices measured along strike of the faults.

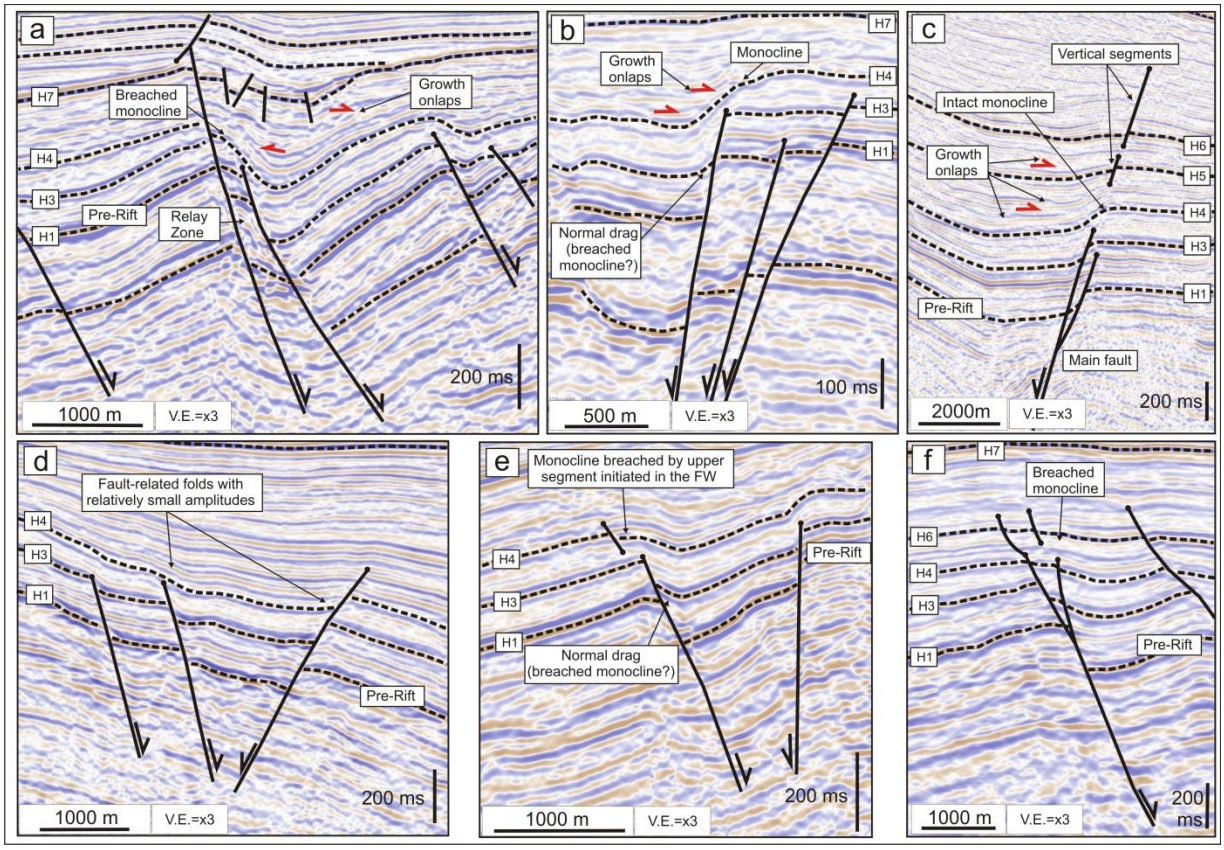

Figure 12. Examples of fault-propagation folds associated with different sets of "simple" and "conjugate" normal faults, interpreted from regional 2D seismic profiles across the IMF (see text for explanations).

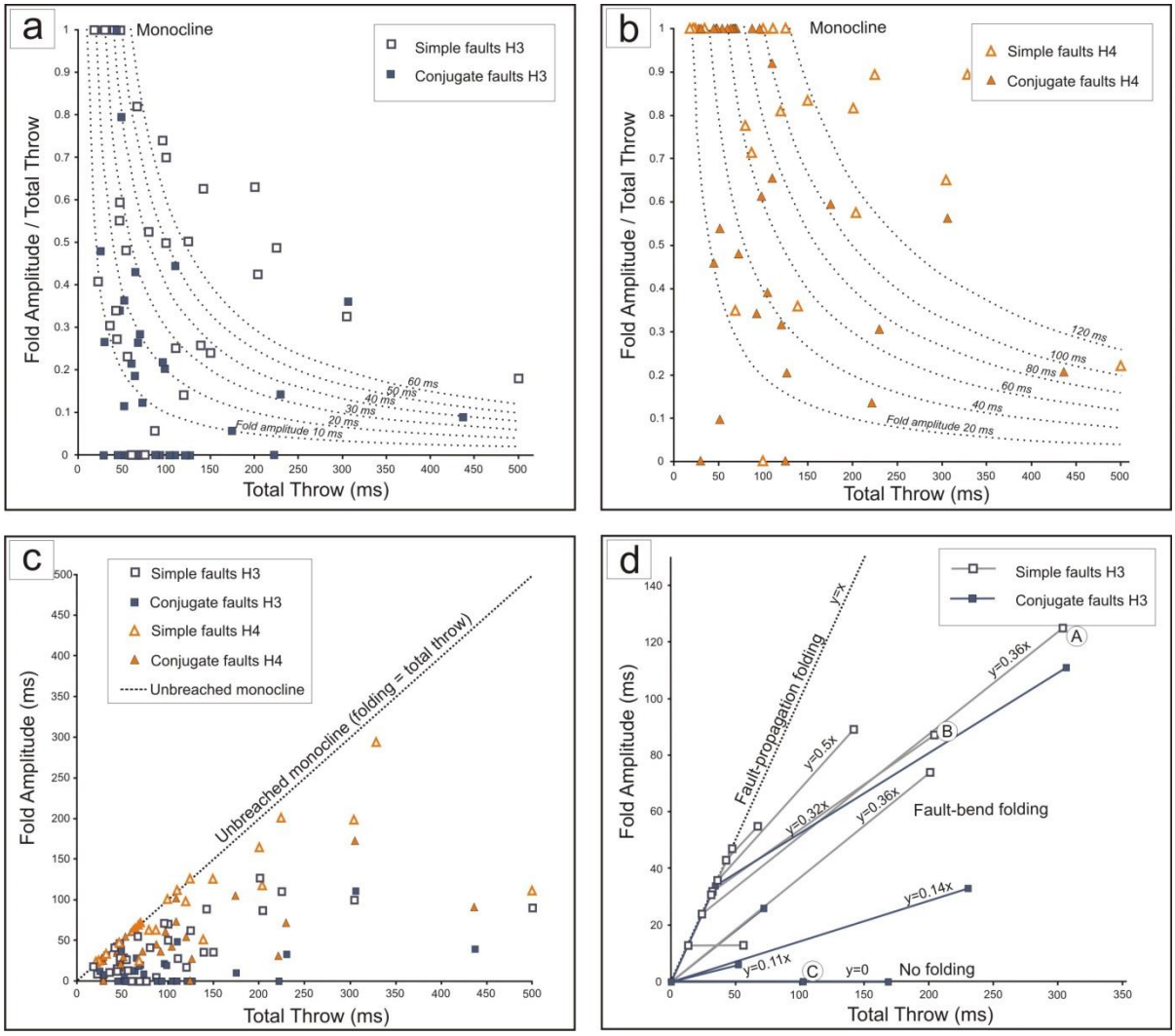

Figure 13 a. Ratio of fold amplitude to total throw *vs.* total throw for horizon H3 (part of mechanical unit 2) measured on both 2D and 3D seismic data on two types of faults, simple normal faults and conjugate normal faults. **b.** Ratio of fold amplitude to total throw *vs.* total throw for horizon H4 (part of mechanical unit 3). **c.** Fold amplitude *vs.* total throw measured for the two horizons, H3 and H4. **d.** Fold amplitude *vs.* total throw for horizon H3 measured on faults from the 3D seismic data set only. A, B, C are measurement localities for the faults displayed in *Figure 9*. The vectors show possible evolution of folding with increasing fault throw (see text for explanation). Fault-propagation folds are characterized by vectors with a gradient of 1.0 (folding = throw), while fault-bend folds are characterized by vectors with gradients from 0.11 to 0.5. The gradients correlate with the change in fault dip within mechanical unit 2 with higher gradients reflecting a larger change in fault dip (see *Figure 9*).

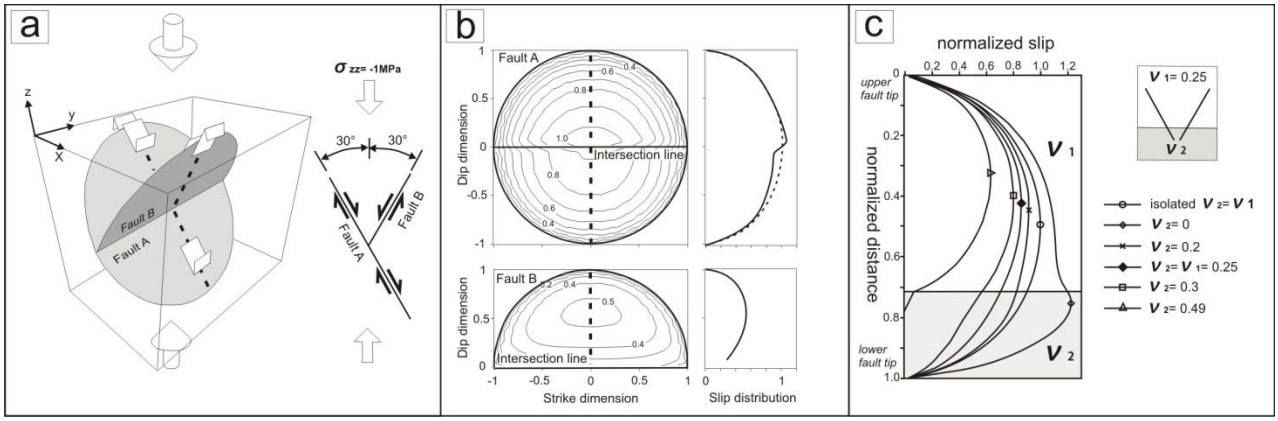

Figure 14. a. Configuration of the elastic boundary element model for conjugate normal faults with a "Y"-type geometry within a homogeneous whole elastic space, from Maerten (1999). **b**. Results of the modelled displacement distribution (Maerten, 1999). **c.** Calculated displacement distributions for conjugate normal faults with a "V"-type geometry located within a heterogeneous elastic material, derived from finite element method modelling (Young, 2001). Note the asymmetric slip distribution, skewed towards the upper fault tip, for models in which the fault intersection lies within a layer that has a higher Poisson's ratio than the surrounding material (i.e. $\nu_2 > \nu_1$).

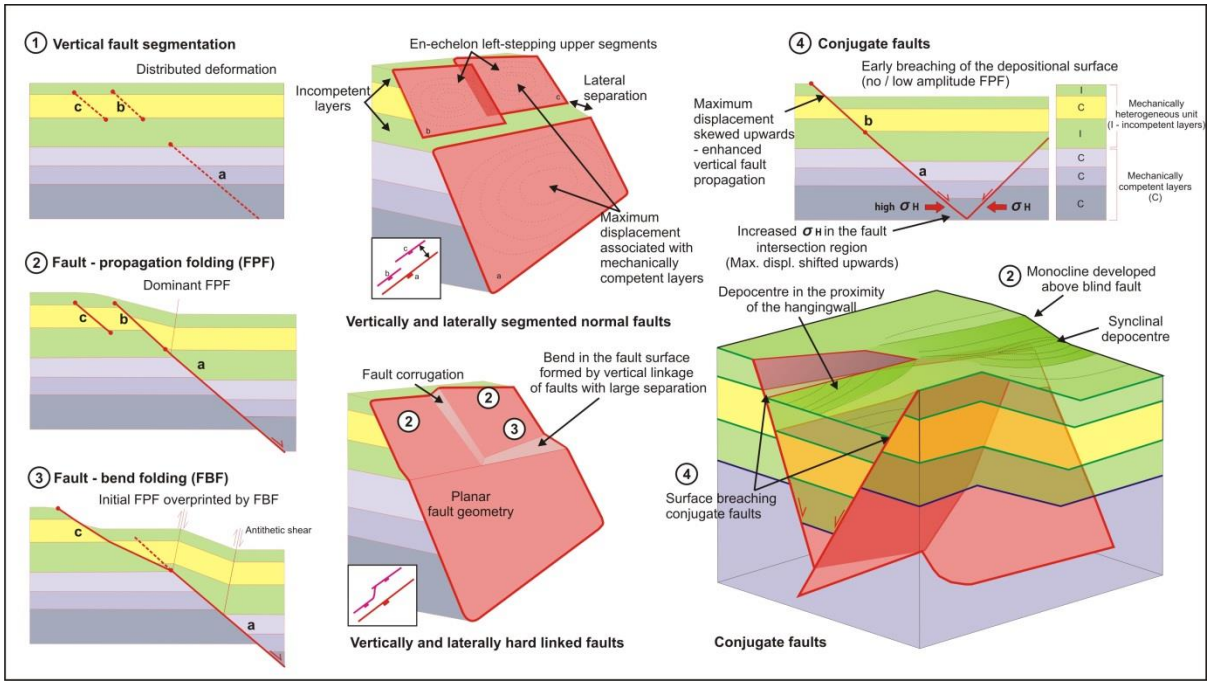

Figure 15. Schematic model summarising the mechanisms responsible for generating spatial and temporal variability in normal fault-related folding within IMF. The heterogeneous sedimentary unit favours fault restriction, segmentation and development of fault-propagation folds (1, 2). Linkage of the main deeper fault with the upper en-echelon segments can generate convex-upward fault geometries and further development of fault-bend folding (3) (modified from Lacazette, 2001). The bend in the fault plane (and the associated folding) is localized and depends on the lateral separation between the upper segments and the main fault. Conjugate faults tend to breach early the depositional surface without developing significant folds ahead of the propagating upper tip (4).

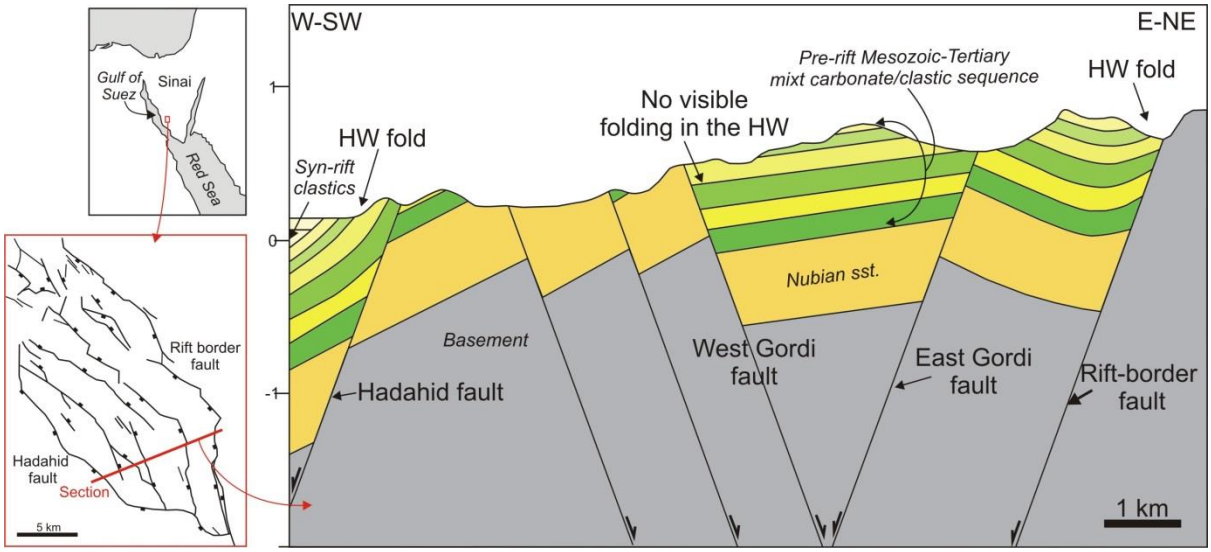

Figure 16. Geological cross-section from Suez Rift (modified from Whipp, 2011). Note the large amplitude hangingwall folds associated with the simple normal faults (Hadahid fault, the rift-border fault). The conjugate West and East Gordi faults display little or no folding in their hangingwalls.